24 Nanoelectromechanical Systems – Experiments and Modeling

Horacio D. Espinosa · Changhong Ke

24.1 Introduction

Nanoelectromechanical systems (NEMS) are made of electromechanical devices that have critical dimensions from hundreds down to a few nanometers. By exploring nanoscale effects, NEMS present interesting and unique characteristics, which deviate greatly from their predecessor microelectromechanical systems (MEMS). For instance, NEMS-based devices can have fundamental frequencies in the microwave range (approximately 100 GHz) [1]; mechanical quality factors in the tens of thousands, meaning low energy dissipation; active mass in the femtogram range [2]; force sensitivity at the attonewton level [3]; mass sensitivity up to attogram [4] and subattogram [5] levels; heat capacities far below a "yoctocalorie" [6]; power consumption in the order of 10 aW [7]; and extremely high integration levels, approaching 10^{12} elements per square centimeter [1]. All these distinguished properties of NEMS devices pave the way for applications such as force sensors, chemical sensors, biological sensors, and ultrahigh frequency resonators.

The interesting properties of the NEMS devices typically arise from the behavior of the active parts, which, in most cases, are in the form of cantilevers or doubly clamped beams with dimensions at the nanometer scale. The materials for these active components include silicon and silicon carbide, carbon nanotubes (CNTs), gold, and platinum, to name a few. Silicon has been the basic material for integrated circuit technology and MEMS during the past few decades, and is widely used to build NEMS as well. Figure 24.1 is a scanning electron microscopy (SEM) image of a double-clamped resonator fabricated from a bulk, single-crystal silicon substrate [8]. However, ultrasmall silicon-based NEMS fail to achieve desired high quality factors owing to the dominance of surface effects, such as surface oxidation

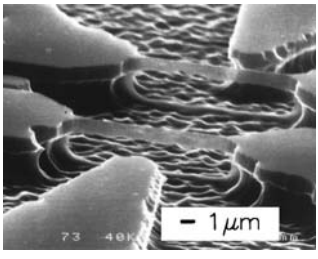

Fig. 24.1. Scanning electron microscope (SEM) image of an undercut Si beam, with length of 7.7 μm, width of 0.33 μm and height of 0.8 μm. (Reprinted with permission from Cleland et al. [8]. Copyright 1996, American Institute of Physics)

and reconstruction, and thermoelastic damping. Limitations in strength and flexibility also compromise the performance of silicon-based NEMS actuators. Instead, CNTs can well represent the ideas of NEMS given their nearly one-dimensional structures with high aspect ratio and perfectly terminated surfaces and excellent electrical, mechanical, and chemical properties. Owing to significant advances in growth, manipulation, and knowledge of their electrical and mechanical properties, CNTs have become the most promising building blocks for the next generation of NEMS. Several CNT-based functional NEMS devices have been reported so far [1, 3, 9–14]. Similar to CNTs, nanowires are another type of one-dimensional novel nanostructures for building NEMS because of their size and controllable electrical properties.

The purpose of this chapter is to provide a comprehensive review of NEMS devices to date and to summarize the modeling currently being pursued to gain insight into their performance. This chapter is organized as follows. In the first part, we review CNTs and CNT-based NEMS. We also discuss nanowire-based NEMS. In the second part, we present the modeling of NEMS, including multiscale modeling and continuum modeling.

24.2 Nanoelectromechanical Systems

24.2.1 Carbon Nanotubes

CNTs exist as a macromolecule of carbon, analogous to a sheet of graphite rolled into a cylinder. They were discovered by Iijima [15] in 1991 and are a subset of the family of fullerene structures. The properties of the nanotubes depend on the atomic arrangement (how the sheets of graphite are rolled to form a cylinder), their diameter, and length. They are light, stiff, flexible, thermally stable, and chemically inert. They have the ability to be either metallic or semiconducting depending on the "twist" of the tube, which is called the "chirality" or "helicity". Nanotubes may exist as either single-walled or multiwalled structures. Multiwalled CNTs (MWNTs) (Fig. 24.2b) are simply composed of multiple concentric single-walled CNTs (SWNTs) (Fig. 24.2a) [16]. The spacing between neighboring graphite layers in MWNTs is approximately 0.34 nm. These layers interact with each other via van der Waals forces.

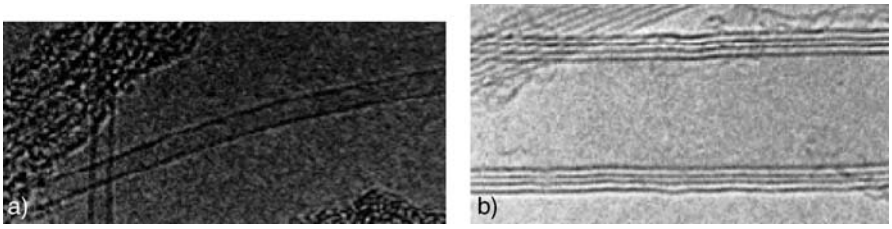

Fig. 24.2. High-resolution transmission electron microscopy image of typical single-walled carbon nanotubes (SWNT) (**a**) and multiwalled carbon nanotubes (MWNT) (**b**). (Reprinted with permission from Ajayan [16] Copyright 1999, American Chemical Society)

The methods used to synthesize CNTs include electric arc discharge [17, 18], laser ablation [19], and catalytic chemical vapor deposition (CVD) [20]. During synthesis, nanotubes are usually mixed with residues including various types of carbon particles. For most applications and tests, a purification process is required. In one of the most common approaches, nanotubes are ultrasonically dispersed in a liquid (e.g., 2-propanol) and the suspension is centrifuged to remove large particles. Other methods, including dielectrophoretic separation, are being developed to provide improved yield.

The mechanical and electrical properties of CNTs have been under intensive study during the past decade. Qian et al. [21] contributed a comprehensive review article from the perspective of both experimentation and modeling. The electronics of CNTs was extensively reviewed by McEuen et al. [22]. Besides, the study of the coupled electromechanical properties, which are essential to NEMS, is rapidly progressing. Some interesting results have been reported regarding the fact that the electrical properties of CNTs are sensitive to the structure variation and can be changed dramatically owing to the change of the atomic bonds induced by mechanical deformations. CNTs can even change from metallic to semiconducting when subjected to mechanical deformation [23–25].

24.2.2 Fabrication Methods

The fabrication processes of NEMS devices can be categorized according to two approaches. *Top-down* approaches, which evolved from manufacturing of MEMS structures, utilize submicron lithographic techniques, such as electron-beam lithography, to fabricate structures from bulk materials, either thin films or bulk substrates. *Bottom-up* approaches fabricate the nanoscale devices by sequential assembly of atoms and molecules as building blocks. Top-down fabrication is size-limited by factors such as the resolution of the electron-beam lithography, etching-induced roughness, and synthesis constraints in epitaxially grown substrates. Significant interest has been shown in the integration of nanoscale materials such as CNTs and nanowires, fabricated by bottom-up approaches, to build nanodevices. Most of the nanodevices reported so far in the literature are obtained by "hybrid" approaches, i.e., combination of bottom-up (self assembly) and top-down (lithographic) approaches [26].

One of the key and most challenging issues of building CNT-based or nanowire-based NEMS is the positioning of nanotubes or nanowires at the desired locations with high accuracy and high throughput. Reported methods of manipulation and positioning of nanotubes are briefly summarized in the following section.

24.2.2.1 Random Dispersion Followed by Electron-Beam Lithography

After purification, a small aliquot of a nanotube suspension is deposited onto a substrate. The result is nanotubes randomly dispersed on the substrate. Nanotubes on the substrate are imaged inside a scanning electron microscope and then this image is digitized and imported to mask-drawing software, where the mask for the subsequent electron-beam lithography is designed. In the mask layout, pads are designed

to superimpose over the ends of the CNTs. Wet etching is employed to remove the material under the CNTs to form freestanding nanotube structures. This process requires an alignment capability in the lithographic step with an accuracy of 0.1 μm or better. This method was first employed to make nanotube structures for mechanical testing [27, 28]. The reported NEMS devices based on this method include nanotube-based rotational actuators [10] and nanowire-based resonators [26].

24.2.2.2 Nanomanipulation

Manipulation of individual CNTs using piezo-driven manipulators inside electron microscope chambers is one of the most commonly used methods to build NEMS [9] and structures for mechanical and electrical testing [29–34]. In general, the manipulation and positioning of nanotubes is accomplished in the following manner: (1) a source of nanotubes is positioned close to the manipulator inside the microscope; (2) the manipulator probe is moved close to the nanotubes under visual surveillance of the microscope monitor until a protruding nanotube is attracted to the manipulator owing to either van der Waals forces or electrostatic forces; (3) the free end of the

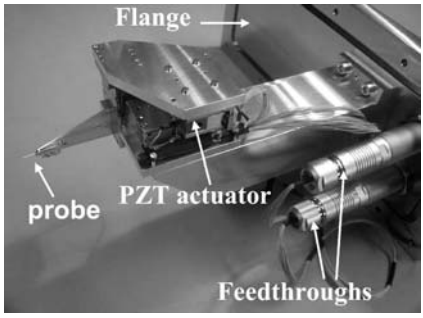

Fig. 24.3. A customized SEM flange holding a three-dimensional nanomanipulator manufactured by Klocke Nanotechnik with two electric feedthroughs, a three-axis piezoelectric transducer (PZT) actuator, and a tungsten probe mounted in the manipulator's probe holder

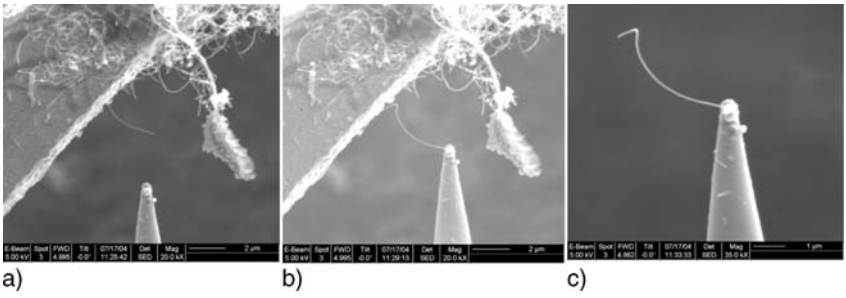

Fig. 24.4. SEM images of the manipulation of carbon nanotubes (CNT) using the 3D Klocke Nanotechnik nanomanipulator. (**a**) Manipulator probe is approaching a protruding nanotube. The sample is a dried nanotube solution on top of a transmission electron microscope (TEM) copper grid. (**b**) Manipulator probe makes contact with the free end of the nanotube and the nanotube is welded to the probe by electron-beam-induced deposition of platinum. (**c**) A single nanotube mounted in the manipulator probe

attracted nanotube is "spot welded" by electron-beam-induced deposition (EBID) of hydrocarbon [9, 34] or metals, like platinum [31], from adequate precursor gases.

Figure 24.3 shows a 3D nanomanipulator (Klocke Nanotechnik, Germany) mounted in a custom-designed scanning electron microscope flange with two electrical feedthroughs, having the capability of moving in X, Y, and Z directions with nanometer-displacement resolution. The manipulation process of an individual CNT is illustrated in Fig. 24.4.

24.2.2.3 External Field Alignment

DC/AC electric fields have been successfully used in the manipulation of nanowires [35], nanotubes [36, 37], and bioparticles [38–40]. Microfabricated electrodes are typically used to create an electric field in the gap between them. A droplet containing CNTs in suspension is dispensed into the gap with a micropipette. The applied electric field aligns the nanotubes, owing to the dielectrophoretic effect, resulting in the bridging of the electrodes by a single nanotube. The voltage drop that arises when the circuit is closed (DC component) ensures the manipulation of only one nanotube. Besides, AC dielectrophoresis has been employed to successfully separate metallic from semiconducting SWNTs in suspension [41]. NEMS devices fabricated using this method include nanotube-based nanorelays [42].

Huang et al. [43] demonstrated another method for aligning nanowires. A laminar flow was employed to achieve preferential orientation of nanowires on chemically patterned surfaces. This method was successfully used in the alignment of silicon nanowires. Magnetic fields have also been used to align CNTs [44].

24.2.2.4 Direct Growth

Rather than manipulating and aligning CNTs after their manufacture, researchers have also examined methods for controlled direct growth. Huang et al. [45] used the microcontact printing (μCP) technique to directly grow aligned nanotubes vertically. Dai et al. [46–49] reported several patterned growth approaches developed in his group. The idea is to pattern the catalyst in an arrayed fashion and control the growth of CNTs from specific catalytic sites. The authors successfully carried out patterned growth of both MWNTs and SWNTs, and exploited methods including self-assembly and external electric field control. Figure 24.5 shows a SEM image of suspended SWNTs grown by an electric-field-directed CVD method [48]. The CNT-based tunable oscillators, reported in [3], were fabricated using this method. Recently, this technique was extended to grow nanotubes in two dimensions to make more complicated nanotube structures, such as nanotube crosses [50].

24.2.2.5 Self-Assembly

Self-assembly is a method of constructing nanostructures by forming stable bonds between the organic or nonorganic molecules and the substrate. Recently, Rao

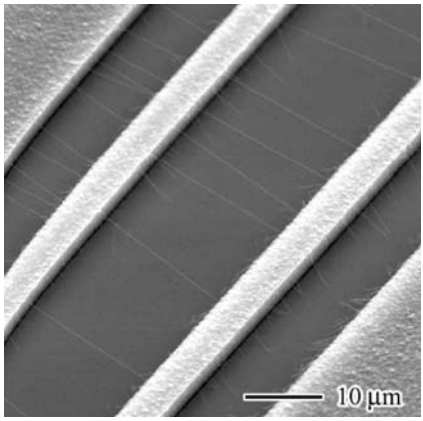

Fig. 24.5. Electric-field-directed freestanding single-walled nanotubes. (Reprinted with permission from Zhang et al. [48]. Copyright 2001, American Institute of Physics)

et al. [51], reported an approach in large-scale assembly of CNTs with high-throughput. Dip-pen nanolithography (DPN), a technique invented by Mirkin's group [52], was employed to functionalize the specific surface regions either with polar chemical groups such as amino ($–NH_2/–NH_3^+$) or carboxyl (–COOH/ $–COO^-$), or with nonpolar groups such as methyl ($–CH_3$). When the substrate with functionalized surfaces was introduced into a liquid suspension of CNTs, the nanotubes were attracted towards the polar regions and self-assembled to form pre-designed structures, usually within 10 s, with a yield higher than 90%. The reported method is scalable to large arrays of nanotube devices by using high-throughput patterning methods such as photolithography, stamping, or massively parallel DPN.

24.2.3 Inducing and Detecting Motion

For nanostructures, both inducing and detecting motion are challenging. Some of the methods routinely used in MEMS face challenges when the size shrinks from microscale to nanoscale. For example, optical methods, such as simple beam deflection schemes or more sophisticated optical and fiber-optical interferometry – both commonly used in scanning probe microscopy to detect the deflection of the cantilevers – generally fall beyond the diffraction limit, which means these methods cannot be applied to objects with cross section much smaller than the wavelength of light [53]. During the past decade, significant progress has been made in nanoscale actuation and detection. Recently, available techniques in the context of NEMS were reviewed [54]. In the following subsections, we summarize these techniques with an emphasis on their accuracy, bandwidth, and limitations.

24.2.3.1 Inducing Motion

Similar to MEMS, electrostatic actuation of nanostructures by an applied electrical field is commonly used for the actuation of NEMS, e.g., nanotweezers [9, 12]. The

Lorenz force has been used to move small conducting beams [8, 26, 55], with alternating currents passing through them in a strong transverse magnetic field. The induced electromotive force (emf), or voltage, can be detected as a measure of the motion. This method requires a fully conducting path and works well with a beam clamped at both ends [56]. Other actuation methods include piezoelectric actuation, thermal actuation using bilayers of materials with different thermal expansion, thermal in-plane actuation due to a specially designed topography [57], and a scanning tunneling microscope (STM) [58].

24.2.3.1.1 Magnetomotive Technique

In magnetomotive induced motion, the actuation force is the Lorenz force produced by current flow through a conductor immersed in a static magnetic field. For example, a doubly clamped beam can be vibrated by flowing a varying current. The beam motion can be either in plane or out of plane depending on the orientation of the beam element with respect to the magnetic field. The Lorenz force acting on the beam is given by

$$F = lBI \ , \tag{24.1}$$

where l is the length of the beam, B is the magnetic field strength, and I is the current going through the beam. The magnetomotive actuation technique is broadband, even in the presence of parasitic capacitance. Huang et al. [59] have recently achieved actuation of a NEMS device in the gigahertz range using this technique.

24.2.3.1.2 Electrostatic Actuation

Electrostatic actuation is widely used in the actuation of MEMS and can also be extended to NEMS. The electrostatic force is calculated from the system capacitance. For instance, the force between two biased parallel plates is given by

$$F = \frac{1}{2} V^2 \frac{\varepsilon A}{d^2} \ , \tag{24.2}$$

where V is the biased voltage, ε is the permittivity (for vacuum, $\varepsilon = 8.854 \times 10^{-12}$ $\mathrm{C^2\,N^{-1}\,m^{-2}}$), A is the area of the plate, and d is the distance between the plates. It is noted that, owing to the presence of parasitic capacitance in MEMS/NEMS, the efficiency of this actuation technique in the high-frequency domain is significantly reduced.

24.2.3.2 Detecting Motion

The most straightforward method is by direct observation of the motion under electron microscopes [9, 12, 60, 61]. This visualization method, typically having resolution on the nanometer scale, projects the motion in the direction perpendicular

to the electron beam. Limitations in depth of focus require that the nano-object motion be primarily in a plane, which normally is coaxial with the electron beam. Electron tunneling is a very sensitive method that can detect subnanometer motion by the exponential dependence of the electron tunneling current on the separation between tunneling electrodes; therefore, this technique is widely used in NEMS motion detection [3, 7]. Magnetomotive detection is a method based on the presence of a magnetic field, either uniform or spatially inhomogeneous, through which a conductor is moved. The time-varying flux generates an induced emf in the loop, which is proportional to the motion [26, 55, 62–64]. The displacement-detection sensitivity of this technique is less than 1 Å [65]. It is known that CNTs can act as transistors, and as such they can be utilized to sense their own motion [3, 66]. Capacitance sensors have been widely used in MEMS. They can also be used in NEMS motion sensing with a resolution of a few nanometers [57], and the resolution can potentially be increased to the angstrom range provided that the capacitance measurement can be improved by 1 order of magnitude. Piezoresistive and piezoelectric detection are techniques capable of sensing minute motion in NEMS by utilizing the material's sensitivity to strain. A material is piezoresistive if its resistance changes with strain. A material is piezoelectric if the electrical polarization changes with deformation. Optical interferometry, in particular, path-stabilized Michelson interferometry and Fabry–Perot interferometry, has been recently developed to detect motion in NEMS [67–71]. For the path-stabilized Michelson interferometric technique, a tightly focused laser beam reflects from the surface of a NEMS device in motion and interferes with a stable reference beam. For the Fabry–Perot interferometric technique, the optical cavity formed within the sacrificial gap between the NEMS surface and the substrate modulates the optical signal on a photodetector as the NEMS device moves in the out-of-plane direction. In the following subsections, we will discuss, in detail, some of the aforementioned displacement-detection techniques and their sensitivities due to the noise level in the system.

24.2.3.2.1 Magnetomotive Technique

The magnetomotive displacement-detection technique is based on the presence of a static magnetic field, through which a conducting nanomechanical element is moved. The time-varying flux induces an emf in the loop, which can be detected by the electrical circuit. For a doubly clamped beam, the generated emf is given by

$$v = \xi B l \dot{x}(t) \ , \tag{24.3}$$

where l is the length of the beam, B is the magnetic field strength. ξ is a geometric factor (for a doubly clamped beam, $\xi \approx 0.885$), and $x(t)$ is the motion of the beam element. A low-noise amplifier is typically employed to enlarge the small emf resulting from minute displacements. The coupling of a magnetomotive transducer to an amplifier is illustrated in Fig. 24.6 [54], which employs a standard amplifier model with two uncorrelated noise sources: a voltage and a current noise source with respective power spectral densities $S_{\mathrm{V}}(\omega)$ and $S_{\mathrm{I}}(\omega)$. Therefore,

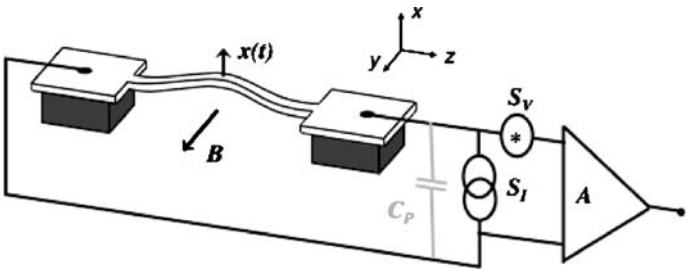

Fig. 24.6. Magnetomotive displacement detection. (Reprinted with permission from Ekinci [54]. Copyright 2005, Wiley-VCH)

the noise power generated in the amplifier determines the displacement sensitivity as [54]

$$|S_{\mathrm{X}}(\omega)| = \frac{S_{\mathrm{V}}(\omega)}{(\xi l B\omega)^2} + \frac{S_{\mathrm{I}}(\omega) l^2 B^2}{m_{\mathrm{eff}}^2 \left(\omega_0^2 - \omega^2\right)^2 + \frac{(\omega\omega_0)^2}{Q^2}} \,, \tag{24.4}$$

where m_{eff} is the effective mass, ω_0 is the resonant frequency, and Q is the quality factor. The first term on the right-hand side in (24.4) is related to the voltage noise in the amplifier, while the second term is related to the current noise in the amplifier.

For displacement measurement using the magnetomotive technique, the bandwidth of motion detection is primarily limited by the parasitic capacitance (C_{p}) in the detection circuit; thus, the cut-off frequency. If the output impedance of a NEMS device is R_{e}, the motion-detection bandwidth of this technique is about $R_{\mathrm{e}} C_{\mathrm{p}}$.

24.2.3.2.2 Electron Tunneling

Electron tunneling is a quantum phenomenon whereby electrons tunnel through a junction in the presence of an electric field. For example, tunneling happens between a very sharp metallic tip and a conductive surface when a subnanometer gap separates the surfaces. This is the principle of scanning electron microscopy. The tunneling current has a very important characteristic: it exhibits an exponential decay as the gap increases, namely,

$$i \approx \rho_{\mathrm{s}}(E_{\mathrm{F}}) V e^{-2kd} \,, \tag{24.5}$$

where i is the current, V is the applied voltage, d is the gap, ρ_{s} (E_{F}) is the local density of electronic states in the test mass, and k is the decay constant for the electron wave function within the gap given by $k = \sqrt{2m_{\mathrm{e}}\phi}/\hbar$; here m_{e} is the mass of the electron, ϕ is the work function of the metal ($\phi \approx 3-5$ eV), and $\hbar$ is Planck's constant divided by 2π. Typically, $k \approx 0.1\ \mathrm{nm}^{-1}$, meaning the current will change an order of magnitude when the gap changes by 1 Å. Therefore, motion information in the element can be converted into an electrical current signal through the tunneling transducer with extremely high sensitivity. Figure 24.7 illustrates a tunneling transducer for displacement detection in NEMS [54]. The motion-detection sensitivity

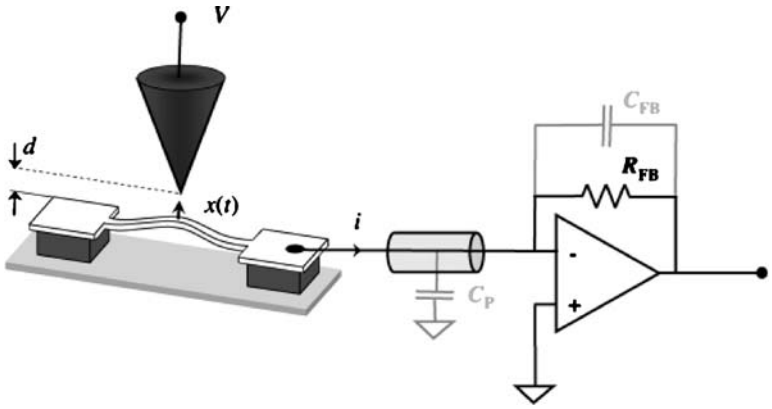

Fig. 24.7. Tunneling transducer for displacement detection in nanoelectromechanical systems (NEMS). (Reprinted with permission from Ekinci [54]. Copyright 2005, Wiley-VCH)

of this technique due to the various sources of noise in the measurement is given by [72, 73]

$$|S_X(\omega)| = \frac{S_I^{(A)}(\omega)}{(2kI)^2} + \frac{e}{2k^2 I} + \frac{S_F^{(BA)}}{m_{eff}^2\left(\omega_0^2 - \omega^2\right)^2 + \frac{(\omega\omega_0)^2}{Q}} \,. \tag{24.6}$$

The first term on the right-hand side is due to the equivalent current noise of the transimpedance amplifier. The second term arises from the granular nature of the electrical charge.

Tunneling in an atomic-scale junction is inherently a fast phenomenon with a speed greater than 1 GHz [74]; however, owing to the high impedance of the tunneling junction and the presence of unavoidable parasitic capacitance, the bandwidth of this detector is typically much lower than the speeds at which NEMS operate.

24.2.3.2.3 Piezoresistive Detection

Piezoresistive detection utilizes materials that are sensitive to strain from which structure displacements can be deconvoluted. Thin films made of piezoresisitive materials have been integrated into microscale cantilevers to detect their motion. High strain sensitivity has been achieved using semiconductor-based piezoresistors, primarily doped Si [75] or AlGaAs [76]. The shortcoming of this sensing technique is its low bandwidth owing to the high impedance of the sensor beam and the presence of parasitic capacitance. Recently, a down-mixing scheme was developed to detect the motion of NEMS in the high-frequency regime [77]. Figure 24.8a illustrates the difficulties in applying low-frequency techniques to high-frequency piezoresistive NEMS. Figure 24.8b illustrates the scheme used to down-mix the displacement signal to a low-frequency signal. In Fig. 24.8a, the piezoresistor R_c is placed in a bridge

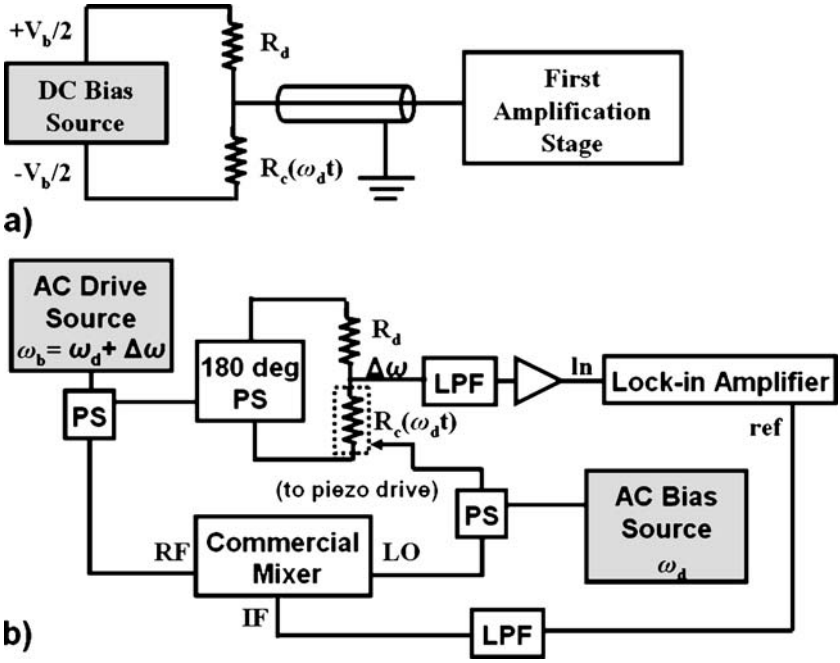

Fig. 24.8. Direct-current bias (**a**) and down-mixing (**b**) circuits. (Reprinted with permission from Bargatin et al. [77] Copyright 2005, American Institute of Physics)

configuration with a fixed dummy resistor R_d. Assuming $R_\mathrm{c} = R_\mathrm{d} = R$, the voltage output from the bridge is zero when the ends of the resistors are oppositely DC-biased at $+V_\mathrm{b}/2$ and $-V_\mathrm{b}/2$. When the NEMS is driven at frequency ω_d, the resistance R_c also has a time-dependent component: $R_\mathrm{c} = R + \Delta R\cos(\omega_\mathrm{d}t + \phi)$; therefore, the voltage output from the bridge is $V_\mathrm{out} \approx V_\mathrm{b}(\Delta R/4R)\cos(\omega_\mathrm{d}t + \phi)$. To measure V_out the bridge output has to be connected in some way to a measuring circuit, such as the input of a preamplifier. At moderately high frequencies (below 30 MHz), this introduces a capacitance C_par in parallel with the cantilever and the dummy resistor, effectively forming a low-pass filter with a cutoff frequency of $(\pi RC_\mathrm{par})^{-1}$. For a typical amplifier input resistance $R > 10\,\mathrm{k}\Omega$ and a cable capacitance $C_\mathrm{par} > 10\,\mathrm{pF}$, the output voltage V_out is strongly attenuated at frequencies of $\omega_\mathrm{d}/2\pi > 2\,\mathrm{MHz}$. For the circuit shown in Fig. 24.8b, an AC voltage $V_\mathrm{b}(t) = V_\mathrm{b0}\cos(\omega_\mathrm{b}t)$ is applied across the resistors at a frequency ω_b, which offsets the drive frequency by an amount $\Delta\omega \equiv \omega_\mathrm{b} - \omega_\mathrm{d}$. Using a 180° power splitter, we apply the voltage oppositely to the ends of the resistors to null the biased voltage at the bridge point. The bias produces an AC current $I(t) = V_\mathrm{b0}\cos(\omega_\mathrm{b}t)/(R_\mathrm{d} + R_\mathrm{c})$. V_out then becomes

$$
\begin{aligned}
V_\mathrm{out}(t) &\approx \frac{V_\mathrm{b0}\cos(\omega_\mathrm{b}t)}{4R}(\Delta R\cos(\omega_\mathrm{d}t + \phi)) \\
&= V_\mathrm{b0}\frac{\Delta R}{8R}\left[\cos(\Delta\omega t - \phi) + \cos((2\omega_\mathrm{d} + \Delta\omega)t + \phi)\right] . \qquad (24.7)
\end{aligned}
$$

From (24.7), the output signal V_{out} has two frequency components given by the sum and the difference of the biased and the drive frequency. With $\Delta\omega$ sufficiently small, the down-mixed frequency is attenuated minimally by the capacitance C_{par}. Using this piezoresistive signal down-mixing scheme, Bargatin et al. [77] demonstrated the motion detection of NEMS cantilevers with fundamental mode frequencies in the 20-MHz range.

24.2.4 Functional NEMS Devices

In this section, we review the CNT- or nanowire-based NEMS devices reported in the literature with a special emphasis on fabrication methods, working principles, and applications.

24.2.4.1 CNT-Based NEMS Devices

24.2.4.1.1 Nonvolatile Random Access Memory

A CNT-based nonvolatile random access memory (NRAM) reported by Rueckes et al. [1] is illustrated in Fig. 24.9a. The device is a suspended SWNT crossbar array for both input/output and switchable, bistable device elements with well-defined off and on states. This crossbar consists of a set of parallel SWNTs or nanowires (lower) on a substrate composed of a conducting layer [e.g., highly doped silicon (dark gray)] that terminates in a thin dielectric layer [e.g., SiO_2 (light gray)], and a set of perpendicular SWNTs (upper) suspended on a periodic array of inorganic

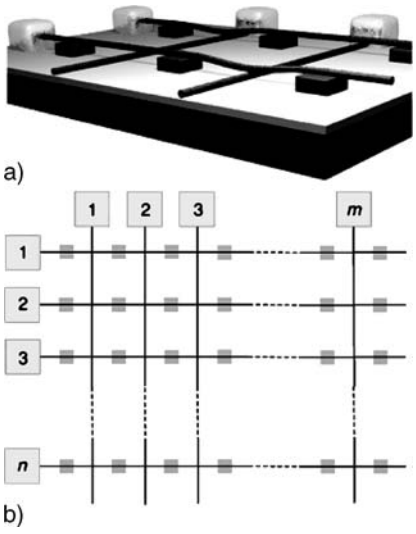

Fig. 24.9. Freestanding nanotube device architecture with multiplex addressing. (**a**) Three-dimensional view of a suspended crossbar array showing four junctions with two elements in the on (contact) state and two elements in the off (separated) state. (**b**) Top view of an *n* by *m* device array. (Reprinted with permission from Rueckes et al. [1] Copyright 2000, American Association for the Advancement of Science)

or organic supports. Each nanotube is contacted by a metal electrode. Each cross point in this structure corresponds to a device element with a SWNT suspended above a perpendicular nanoscale wire. Qualitatively, bistability can be envisioned as arising from the interplay of the elastic energy and the van der Waals energy when the upper nanotube is freestanding or the suspended SWNT is deflected and in contact with the lower nanotube. Because the nanotube junction resistance depends exponentially on the separation gap, the separated upper-to-lower nanotube junction resistance will be orders of magnitude higher than that of the contact junction; herefore, two states, "off" and "on," are well defined. For a device element, these two states can be read simply by measuring the resistance of the junction and, moreover, can be switched between off and on states by applying voltage pulses to nanotubes through the corresponding electrodes to produce attractive or repulsive electrostatic forces. A key aspect of this device is that the separation between top and bottom conductors must be on the order of 10 nm. In such a case, the van der Waals energy overcomes the elastic energy when the junction is actuated (on state) and remains on this state even if the electrical field is turned off (nonvolatile feature).

In the integrated system, electrical contacts are made only at one end of each of the lower and upper sets of nanoscale wires in the crossbar array, and thus many device elements can be addressed from a limited number of contacts (Fig. 24.9b). This approach suggests a highly integrated, fast, and macroscopically addressable NRAM structure that could overcome the fundamental limitations of semiconductor RAM in size, speed, and cost. Integration levels as high as 1×10^{12} elements per square centimeter and switching time down to approximately 5 ps (200-GHz operation frequency) using 5-nm device elements and 5-nm supports are envisioned while maintaining the addressability of many devices through the long (approximately 10-μm) SWNT wires. However, such small dimensions, in particular, the junction gap size, impose significant challenges in the nanofabrication of parallel device arrays.

24.2.4.1.2 Nanotweezers

There are two types of CNT-based nanotweezers: those reported by Kim and Lieber [12] in 1999 and Akita et al. [9] in 2001. Both nanotweezers employ MWNTs as the tweezers' arms which are actuated by electrostatic forces. Applications of these nanotweezers include the manipulation of nanostructures and two-tip STM or atomic force microscope (AFM) probes [12].

The fabrication process of the CNT-based nanotweezers reported by Kim and Lieber [12] is illustrated in Fig. 24.10a. Freestanding electrically independent electrodes were deposited onto tapered glass micropipettes with end diameters of 100 nm (Fig. 24.10b). MWNT or SWNT bundles with diameters of 20–50 nm were attached to the two gold electrodes under the direct view of an optical microscope operated in dark-field mode using an adhesive [78, 79]. A scanning electron microscope image of fabricated nanotube tweezers is shown in Fig. 24.10c. The gap between the two nanotweezers' arms was controlled by the applied bias voltage between the electrodes. The nanotube nanotweezers have been demonstrated successfully to

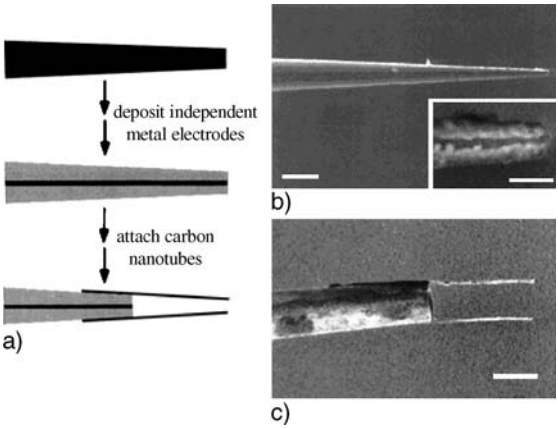

Fig. 24.10. Overview of the fabrication of CNT nanotweezers. (**a**) The deposition of two independent metal electrodes and the subsequent attachment of CNTs to these electrodes. (**b**) SEM image of the end of a tapered glass structure after the two deposition steps. *Scale bar* 1 μm. The higher-resolution *inset* shows clearly that the electrodes are separated. *Scale bar* 200 nm. (**c**) SEM image of nanotweezers after mounting two MWNT bundles on each electrode. *Scale bar* 2 μm. (Reprinted with permission from Kim et al. [12]. Copyright 1999, American Association for the Advancement of Science)

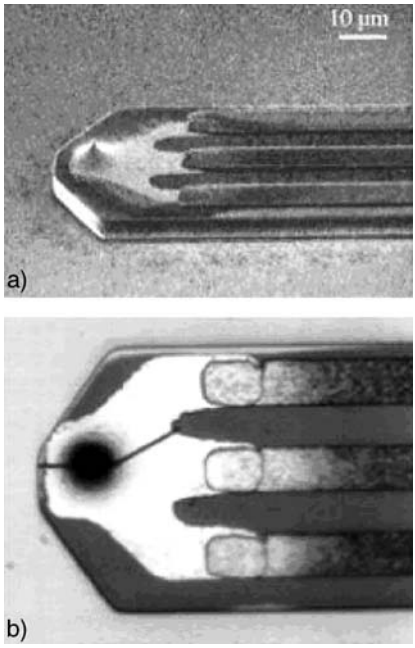

Fig. 24.11. SEM images of a Si cantilever as a base for nanotube nanotweezers. (**a**) A Ti/Pt film was coated on the tip and connected to three Al lines patterned on the cantilever. (**b**) The Ti/Pt film was separated into two by a focused ion beam and these two were connected to one and two Al lines, respectively. (Reprinted with permission from Akita et al. [9]. Copyright 2001, American Institute of Physics)

manipulate nanostructures, such as fluorescently labeled polystyrene spheres and a β-SiC nanocluster, and GaAs nanowires [12].

The CNT-based nanotweezers reported by Akita et al. [9], are shown in Fig. 24.11. Commercially available Si AFM cantilevers were employed as the device body. A Ti/Pt film was coated on the tip of the cantilever and connected to three Al interconnects that were patterned on the cantilever by a conventional lithographic technique as shown in Fig. 24.11a. The Ti/Pt film was separated into two by focused ion beam (FIB) etching. These two parts were independently connected to Al interconnects as shown in Fig. 24.11b. DC voltage was applied between the separated Ti/Pt tips through the Al interconnect, to operate the tweezers after attaching two arms of nanotubes to them using a three-stage manipulator. Figure 24.12a shows an SEM image of a typical pair of nanotube nanotweezers with a cantilevers length of about 2.5 μm and the separation between their tips of about 780 nm.

The operation of the nanotube nanotweezers was examined by in situ SEM. Various voltages were applied between the two arms to get them to close owing to the electrostatic attraction force. Figure 24.12b–d shows the motion of the nanotube arms as a function of the applied voltage V. It is clearly seen that the arms bent and the separation between the tips decreased with increasing applied voltage. The separation became 500 nm at $V = 4$ V and zero at $V > 4.5$ V. It is noted that the motion in Fig. 24.12 could be repeated many times without permanent deformation, suggesting that CNTs are ideal materials for building NEMS.

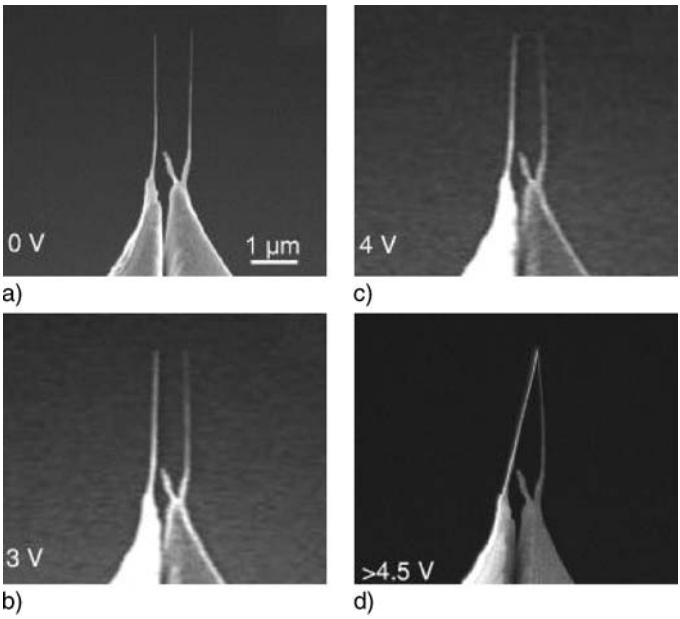

Fig. 24.12. SEM images of the motion of nanotube arms in a pair of nanotweezers as a function of the applied voltage. (Reprinted with permission from Akita et al. [9]. Copyright 2001, American Institute of Physics)

24.2.4.1.3 Rotational Motors

A CNT-based rotational motor reported by Fennimore et al. [10] in 2003 is conceptually illustrated in Fig. 24.13a. The rotational element (R), a solid rectangular metal plate serving as a rotor, is attached transversely to a suspended support shaft. The ends of the support shaft are embedded in electrically conducting anchors (A1, A2) that rest on the oxidized surface of a silicon chip. The rotor plate assembly is surrounded by three fixed stator electrodes: two "in-plane" stators (S1, S2) are horizontally opposed and rest on the silicon oxide surface, while the third "gate" stator (S3) is buried beneath the surface. Four independent (DC and/or appropriately phased AC) voltage signals, one applied to the rotor plate and three to the stators, are applied to control the position, speed, and direction of rotation of the rotor plate. The key component in the assembly is a single MWNT, which serves simultaneously as the rotor plate support shaft and the electrical feedthrough to the rotor plate; most importantly it is also the source of rotational freedom.

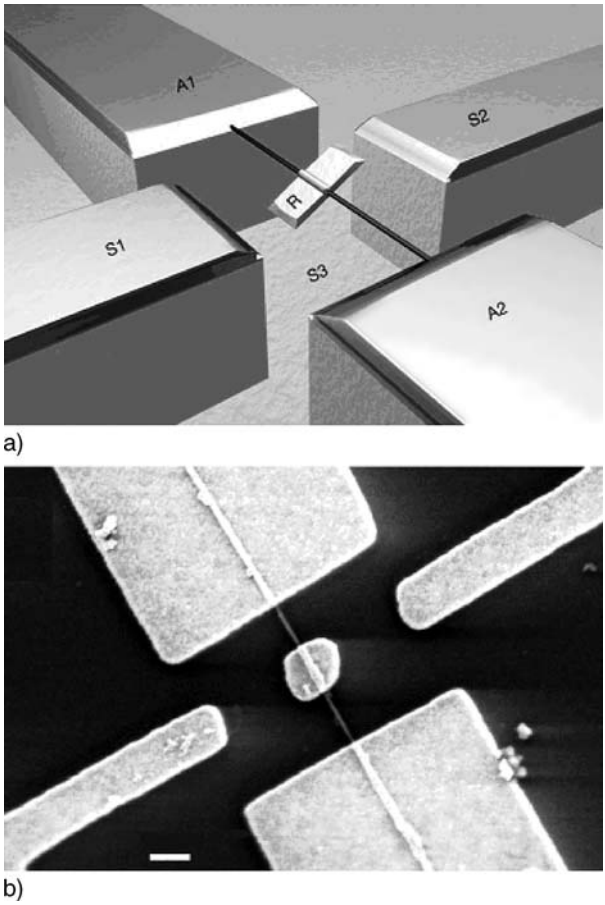

Fig. 24.13. Integrated synthetic NEMS actuator. (**a**) Conceptual drawing of nanoactuator. (**b**) SEM image of nanoactuator just prior to HF etching. *Scale bar* 300 nm. (Reprinted with permission from Fennimore et al. [10]. Copyright 2003, Nature Publishing Group)

The nanoactuator was constructed using lithographic methods. MWNTs in suspension were deposited on a doped silicon substrate covered with 1 μm of SiO_2. The nanotubes were located using an AFM or a scanning electron microscope. The remaining actuator components (in-plane rotor plate, in-plane stators, anchors, and electrical leads) were then patterned using electron-beam lithography. A HF etch was used to remove roughly 500 nm of the SiO_2 surface to provide clearance for the rotor plate. The conducting Si substrate here serves as the gate stator. Figure 24.13b shows an actuator device prior to etching. Typical rotor plate dimensions were 250–500 nm on a side.

The performance of the nanoactuator was examined in situ inside the scanning electron microscope chamber. Visible rotation could be obtained by applying DC voltages up to 50 V between the rotor plate and the gate stator. When the applied voltage was removed, the rotor plate would rapidly return to its original horizontal position. To exploit the intrinsic low-friction-bearing behavior afforded by the perfectly nested shells of MWNTs, the MWNT supporting shaft was modified in situ by successive application of very large stator voltages. The processes resulted in fatigue and eventually shear failure of the outer nanotube shells. In the "free" state, the rotor plate was still held in position axially by the intact nanotube core shells, but could be azimuthally positioned, using an appropriate combination of stator signals,

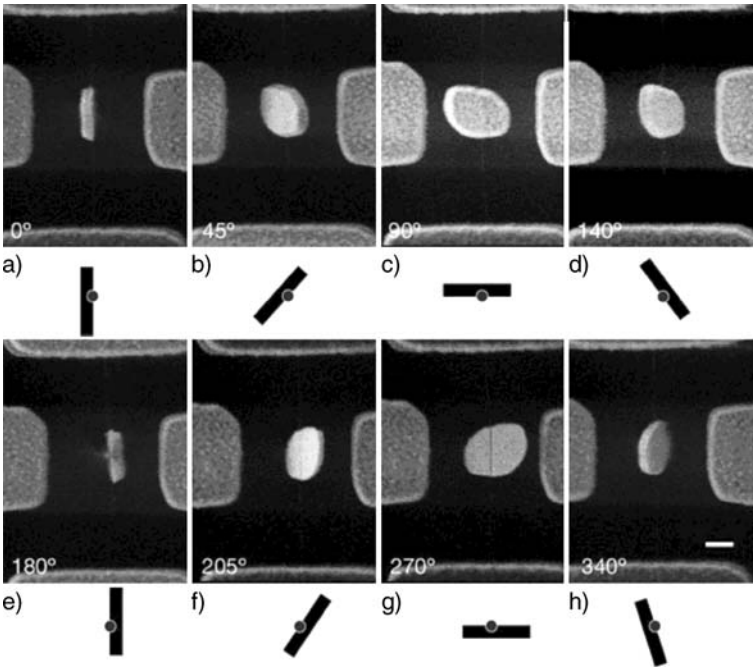

Fig. 24.14. Series of SEM images showing the actuator rotor plate at different angular displacements. The schematic diagrams located *beneath* each SEM image illustrate a cross-sectional view of the position of the nanotube/rotor-plate assembly. *Scale bar* 300 nm. (Reprinted with permission from Fennimore et al. [10]. Copyright 2003, Nature Publishing Group)

to any arbitrary angle between 0 and 360°. Figure 24.14 shows a series of still SEM images, recorded from an actuated device in the free state, being "walked" through one complete rotor plate revolution using quasi-static DC stator voltages. The stator voltages were adjusted sequentially to attract the rotor plate edge to successive stators. Reversal of the stator voltage sequence allowed the rotor plate rotation to be reversed in an equally controlled fashion. The experiments show that the MWNT clearly serves as a reliable, presumably wear free, NEMS element providing rotational freedom. No apparent wear or degradation in performance was observed after many thousands of cycles of rotations.

Potential applications of the MWNT-based actuators include ultra-high-density optical sweeping and switching elements, paddles for inducing and/or detecting fluid motion in microfluidics systems, gated catalysts in wet chemistry reactions, biomechanical elements in biological systems, or general (potentially chemically functionalized) sensor elements.

24.2.4.1.4 Nanorelays

CNT-based nanorelays were first reported by Kinaret et al. [13] in 2003 and were later demonstrated experimentally by Lee et al. [42] in 2004. The nanorelay is a three-terminal device including a conducting CNT placed on a terrace in a silicon substrate and connected to a fixed source electrode (S), as shown in Fig. 24.15a. A gate electrode (G) is positioned underneath the nanotube so that charge can be induced in the nanotube by applying a gate voltage. The resulting capacitance force q between the nanotube and the gate bends the tube and brings the tube end into contact with a drain electrode (D) on the lower terrace, thereby closing an electric circuit. Theoretical modeling of the device shows that there is a sharp transition from a nonconducting (off) to a conducting (on) state when the gate voltage is varied at a fixed source-drain voltage. The sharp switching curve allows for amplification of weak signals superimposed on the gate voltage [13].

One fabricated nanorelay device is shown in Fig. 24.15b. A MWNT was positioned on top of the source, gate, and drain electrodes with poly(methyl methacrylate) (PMMA) as a sacrificial layer using AC-electrophoresis techniques [36]. Then, a top electrode was placed over the nanotube at the source to ensure good contact. The underlying PMMA layer was then carefully removed to produce a nanotube suspended over the gate and drain electrodes. The separation between gate and drain was approximately 250 nm and the source–drain distance was 1.5 μm.

The electromechanical properties of nanotube relays were investigated by measuring the current–gate voltage (I–V_{sg}) characteristics, while applying a source–drain voltage of 0.5 V. Figure 24.16 shows the I–V_{sg} characteristics of one of the nanotube relays with an initial height difference between the nanotube and drain electrode of approximately 80 nm. The drain current started to increase nonlinearly when the gate voltage reached 3 V (at this gate voltage the current is in the order of 10 nA). The nonlinear current increase was a signature of electron tunneling as the distance between the nanotube and the drain electrode was decreased. Beyond $V_{sg} = 20$ V there was a change in the rate of current increase. With the current increase rate becoming more linear, strong fluctuations could be detected. The deflection of the nanotube

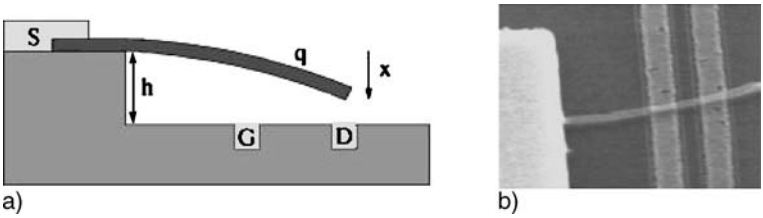

Fig. 24.15. A CNT nanorelay device (**a**) and a SEM image of a fabricated nanorelay device (**b**) ((**a**) Reprinted with permission from Kinaret et al. [13]. Copyright 2002, American Institute of Physics. (**b**) Reprinted with permission from Lee et al. [42]. Copyright 2004, American Chemical Society)

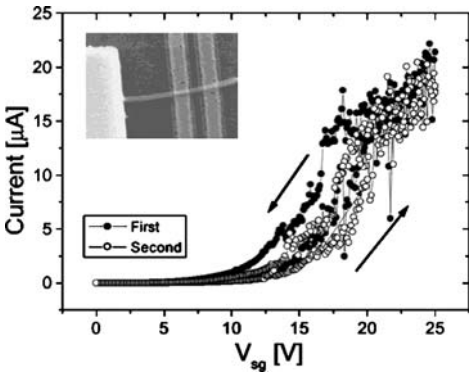

Fig. 24.16. I–V_{sg} characteristics of a nanotube relay initially suspended approximately 80 nm above the gate and drain electrodes. (Reprinted with permission from Lee et al. [42] Copyright 2004, American Chemical Society)

was found to be reversible. The current decreased with the reduction of gate voltage, showing some hysteresis, until it reached zero for a gate voltage below 3 V. The current measured during the increasing V_{sg} part of the second scan closely followed that of the first scan, especially in the region below $V_{sg} = 12$ V. The dynamics of the nanorelays was recently investigated by Jonsson et al. [80]. The results show that the intrinsic mechanical frequencies of nanorelays are in the gigahertz regime and the resonance frequency can be tuned by the biased voltage.

The potential applications of nanorelays include memory elements, pulse generators, signal amplifiers, and logic devices.

24.2.4.1.5 Feedback-Controlled Nanocantilevers

A feedback-controlled CNT-based NEMS device reported by Ke and Espinosa [11] in 2004, schematically shown in Fig. 24.17, is made of a MWNT placed as a cantilever over a microfabricated step. A bottom electrode, a resistor, and a power supply are parts of the device circuit. When a voltage $U < V_{PI}$ (*pull-in* voltage) is applied, the resulting electrostatic force is balanced by the elastic force from the deflection of the nanotube cantilever. The nanotube cantilever remains in the "upper" equilibrium position. When the applied voltage exceeds the pull-in voltage, the electrostatic force becomes larger than the elastic force and the nanotube accelerates towards the

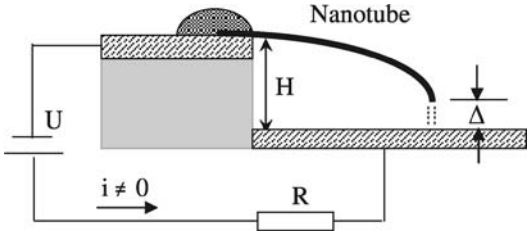

Fig. 24.17. Nanotube-based device with tunneling contact. (Reprinted with permission from Ke et al. [11]. Copyright 2004, American Institute of Physics)

bottom electrode. When the tip of the nanotube is very close to the electrode (i.e., gap $\Delta \approx 0.7\,\text{nm}$), as shown in Fig. 24.17, a substantial tunneling current passes between the tip of the nanotube and the bottom electrode. Owing to the existence of the resistor in the circuit, the voltage applied to the nanotube drops, weakening the electric field. Because of the kinetic energy of the nanotube, it continues to deflect downward and the tunneling current increases, weakening the electric field further. In this case, the elastic force is larger than the electrostatic force and the nanotube decelerates and eventually changes the direction of motion. This decreases the tunneling current and the electrical field recovers. If there is damping in the system, the kinetic energy of the nanotube is dissipated and the nanotube stays at the position where the electrostatic force is equal to the elastic force, and a stable tunneling current is established in the device. This is the "lower" equilibrium position for the nanotube cantilever. At this point, if the applied voltage U decreases, the cantilever starts retracting. When U decreases to a certain value, called the *pull-out* voltage V_{PO}, the cantilever is released from its lower equilibrium position and returns back to its upper equilibrium position. At the same time, the current in the device diminishes substantially. Basically the pull-in and pull-out processes follow a hysteretic loop for the applied voltage and the current in the device. The upper and lower equilibrium positions correspond to "on" and "off" states of a switch, respectively. The existence of the tunneling current and feedback resistor make the "lower" equilibrium state very robust, which is key to some applications of interest. The representative characteristic curve of the device is shown in Fig. 24.18: Fig. 24.18a shows the relation between the gap Δ and the applied voltage U; Fig. 24.18b shows the relation between the current i in the circuit and the applied voltage U. The potential applications of the device include ultrasonic wave detection for monitoring the health of materials and structures, gap sensing, NEMS switches, memory elements, and logic devices.

In comparison with nanorelays [13, 42], the device reported in [11] is a two-terminal device, providing more flexibility in terms of device realization and control than the nanorelay. In comparison with the NRAM described in [1], the feedback-controlled device employs an electrical circuit incorporated with a resistor to adjust the electrostatic field to achieve the second stable equilibrium position. This feature reduces the constraints in fabricating devices with nanometer-gap control between the free standing CNTs or nanowires and the substrate, providing more reliability and tolerance to variability in fabrication parameters. However, the drawback of the device in memory applications is that the memory becomes volatile. The working principle and the potential applications for these two devices are somewhat complementary.

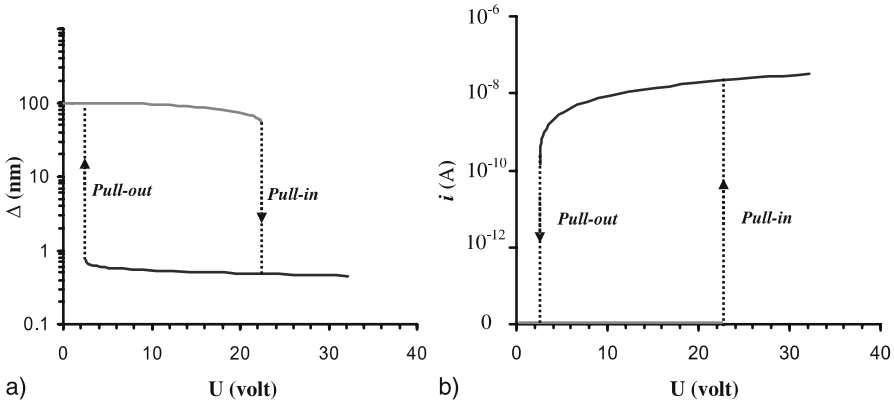

Fig. 24.18. Representative characteristic of pull-in and pull-out processes for the feedback-controlled nanocantilever device. (**a**) Relationship between the gap Δ and the applied voltage U. (**b**) Relationship between the current i in the circuit and the applied voltage U. (Reprinted with permission from Ke et al. [11]. Copyright 2004, American Institute of Physics)

Recently the electromechanical behavior of the feedback-controlled NEMS device was demonstrated experimentally by in situ SEM testing [81]. The test configuration employed is schematically shown in Fig. 24.19a [81, 82]. By employing a three-axes nanomanipulator (Klocke Nanotechnik) possessing nanometer positioning accuracy, a MWNT was welded to a tungsten probe tip by EBID of platinum [31]. A second electrode employed in the configuration (Fig. 24.19a) consisted of a silicon chip coated with a 5-nm-thick Cr adhesion layer and a 50-nm Au film. This chip was glued onto the side of a Teflon block and mounted vertically in the scanning electron microscope x–y–z stage. With use of an electric feedthrough, the two electrodes were connected to a resistor, $R = 1\,\mathrm{G}\Omega$, and to a current–voltage electronic measurement unit (Keithley 4200 SCS). The nanotube cantilever welded to the manipulator probe was displaced until a desired distance (typically 0.5–3 μm, depending on the length and the diameter of nanotubes) between the freestanding CNT and Au electrode was reached. The configuration shown in Fig. 24.19a is considered electromechanically equivalent to the proposed device shown in Fig. 24.17. The pull-in behavior of the device (gap–voltage curve), in particular, the pull-in voltage, and the pull-in/pull-out behavior of the device (current–voltage curve) were examined systematically using this testing configuration.

The measured pull-in behavior of a MWNT cantilever 6.8-μm long and with outer diameter of 47 nm placed parallel to the electrode with a gap size of 3 μm and the comparison with the theoretical prediction will be detailed in Sect. 24.3.2.3. Figure 24.19b shows an experimentally measured current–voltage (I–U) curve during the pull-in/pull-out processes and the theoretical prediction for a nanotube 9-μm long [81, 82]. The measured I–U curve exhibited the theoretically predicted bistability and hysteretic loop. The arrows show the direction in which the hysteretic loop traveled during the increase and decrease of the driving voltage U. The measurement exhibits a background noise of about 0.1 pA, which is typical in these measurements.

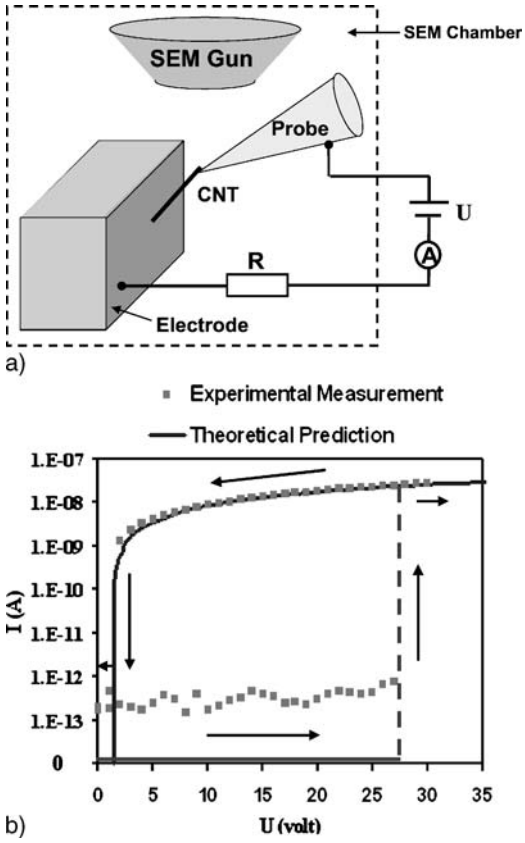

Fig. 24.19. In situ pull-in/pull-out experiments. (**a**) The setup for in situ testing of nanotube cantilever devices. (**b**) Measured *I–U* characteristic curve during the pull-in/pull-out processes and comparison with analytical predictions. The *arrows* show the direction in which the hysteretic loop is described during the increase and decrease of the driving voltage *U*

Depending on the device characteristic dimensions, failure modes were observed in the in situ SEM studies [81, 82]. These dimensions were selected to produce accelerated failure, i.e., the operational conditions were extreme. Figure 24.20a–d illustrates one of the observed failure modes consisting of partial loss of the nanotube cantilever around the tip area after each pull-in/pull-out cycle, i.e., a reduction of nanotube length. This phenomenon has been consistently observed. Detailed examination of Fig. 24.20a–d clearly reveals that the length of the nanotube becomes approximately 1 μm shorter after each pull-in/pull-out event. The gaps between the tip of the nanotube and the electrode for the sequence of pull-in/pull-out tests were controlled to be in the range 0.5–2 μm and the pull-in voltages were found to be in the range 15–30 V. From the various experiments, two possible failure sources are envisioned. One involves CNT fracture as a result of its impact with the bottom electrode during the unstable pull-in event. Another possible source is the sublimation of the CNT as a result of high instantaneous current densities and associated Joule heating. It is important to note that these two damage mechanisms may operate simultaneously. A study on the stability of charged SWNTs using the density functional based tight-binding method (DFTB) provides some insight into these failure modes [83, 84]. The study showed that the ends of nanotubes become unstable as the

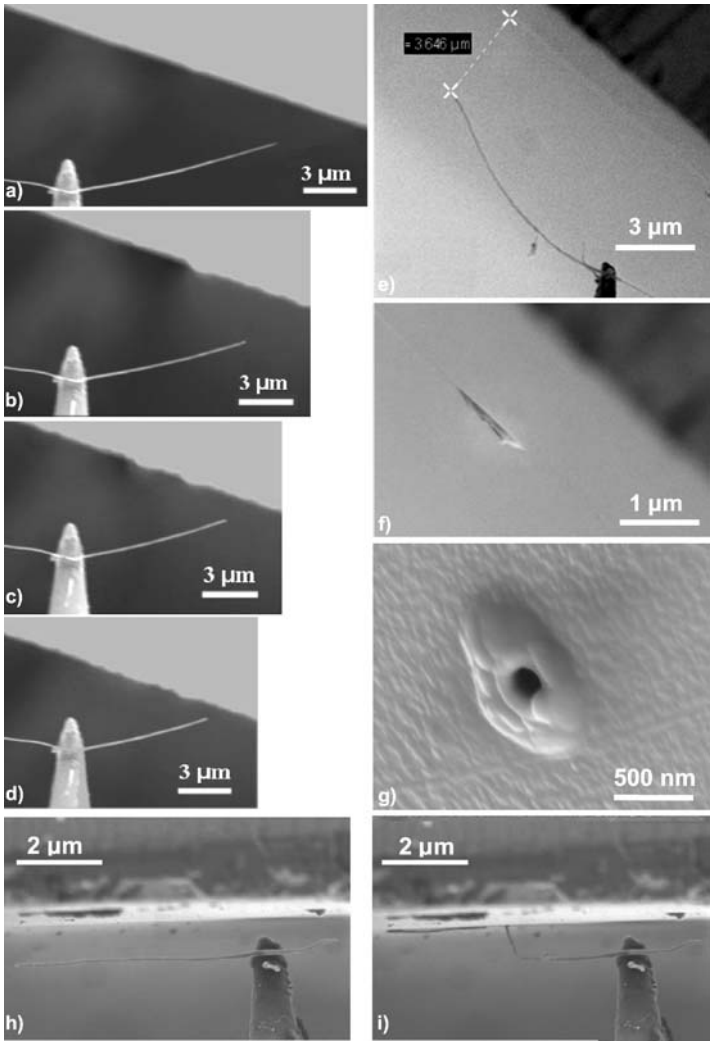

Fig. 24.20. Failure modes of the NEMS device. (**a**)–(**d**) Example of device failure due to partial loss of the nanotube cantilever after each pull-in/pull-out sequence. (**e**)–(**g**) SEM images showing electrode damage and melting at high pull-in voltages. (**h**), (**i**) Fracture of the nanotube cantilever during the pull-in event

electrical charge density is increased. This is the case because charges are concentrated at the ends, eliciting strong repulsive Coulomb electrostatic interactions that tend to eject end atoms. The ejection mechanism may be exacerbated by local mechanical deformation and high temperatures arising from spikes in current densities. Further evidence of the CNT impact and high current densities was obtained from another experiment in which the gap was set to a value of 3.646 µm. Figure 24.20e,f shows SEM images of the device before and after pull-in. It is observed that part

of the electrode surface was damaged when pull-in happened at an applied voltage U of 70 V. Figure 24.20g is a zoom-in view of the damaged electrode area showing a hole formed in the center of the damaged surface area, likely the result of local gold vaporization. The diameter of the hole was measured to be approximately 150 nm, which is a little larger than the diameter of the nanotube (approximately 120 nm). The area around the hole seems "melted" and blistered, probably owing to the rapid thermal expansion and delamination of the gold film as a result of sudden energy release. Figure 24.20h,i illustrates SEM images showing evidence of nanotube fracture. Figure 24.20h shows a nanotube 6.6-μm long and with a diameter of approximately 100 nm placed parallel to the electrode with a gap of 1 μm prior to actuation. When pull-in occurred at a voltage of 19.2 V, part of the nanotube cantilever was broken and remained attached to the Au electrode. The remaining part of the nanotube pulled in again and remained in contact with the electrode, as shown in Fig. 24.20i. All these observations confirm that in order to design reliable NEMS devices it is imperative to gain a basic understanding of failure modes as a function of configuration parameters such that maps with envelops defining reliable operational conditions can be obtained.

24.2.4.1.6 Tunable Oscillators

The fabrication and testing of a tunable CNT oscillator was reported by Sazonova et al. [3]. It consists of a doubly clamped nanotube, as shown in Fig. 24.21. They demonstrated that the resonance frequency of the oscillators can be widely tuned and that the devices can be used to transduce very small forces.

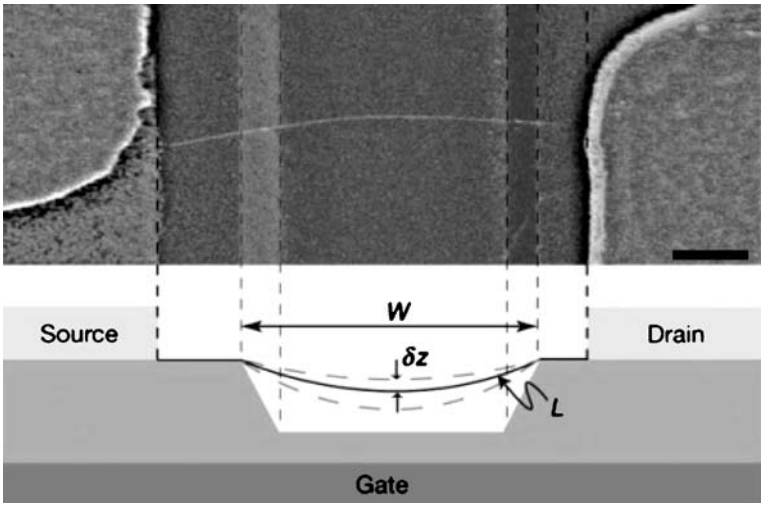

Fig. 24.21. SEM image of a suspended device (*top*) and the device geometry (*bottom*). *Scale bar* 300 nm. The sides of the trench, typically 1.2–1.5-μm wide and 500-nm deep, are marked with *dashed lines*. A suspended nanotube can be seen bridging the trench. (Reprinted with permission from Sazonova et al. [3]. Copyright 2004, Nature Publishing Group)

Single or few-walled nanotubes with diameters in the range 1–4 nm, grown by CVD, were suspended over a trench (typically 1.2–1.5-μm wide, 500-nm deep) between two metal (Au/Cr) electrodes. A small section of the tube resided on the oxide on both sides of the trench; the adhesion of the nanotube to the oxide provided clamping at the end points. The nanotube motion was induced and detected using the electrostatic interaction with the gate electrode underneath the tube. In this device, the gate voltage has both a static (DC) component and a small time-varying (AC) component. The DC voltage at the gate produces a static force on the nanotube that can be used to control its tension. The AC voltage produces a periodic electric force, which sets the nanotube into motion. As the driving frequency approaches the resonance frequency of the tube, the displacement becomes large.

The transistor properties of semiconducting [85] and small-bandgap semiconducting [86,87] CNTs were employed to detect the vibrational motion. Figure 24.22a shows the measured current through the nanotube as a function of driving frequency at room temperature. A distinctive feature in the current on top of a slowly changing background can be seen. This feature is due to the resonant motion of the nanotube, which modulates the capacitance, while the background is due to the modulating gate voltage.

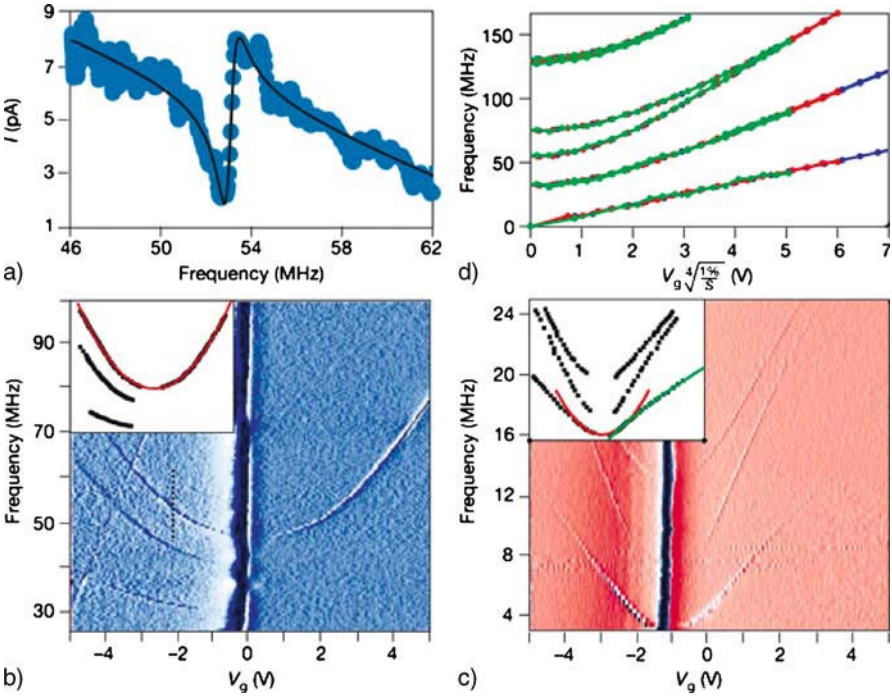

Fig. 24.22. Measurements of resonant response. (**a**) Detected current as a function of driving frequency. (**b**),(**c**) Detected current as a function of gate voltage V_g and frequency for devices 1 and 2. (**d**) Theoretical predictions for the dependence of vibration frequency on gate voltage for a representative device. (Reprinted with permission from Sazonova et al. [3]. Copyright 2004, Nature Publishing Group)

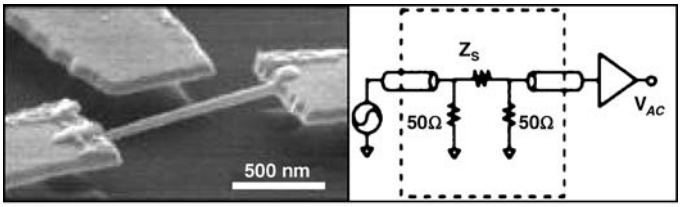

Fig. 24.23. (**a**) SEM image of the suspended nanowire device, 1.3-μm long and 43 nm in diameter. (**b**) Measurement circuit used for magnetomotive drive and detection. (Reprinted with permission from Husain et al. [26]. Copyright 2003, American Institute of Physics)

The DC voltage on the gate can be used to tune the tension in the nanotube and therefore the oscillation frequency. Figure 24.22b,c shows the measured response as a function of the driving frequency and the static gate voltage. The resonant frequency shifts upward as the magnitude of the DC gate voltage is increased. Several distinct resonances are observed, corresponding to different vibrational modes of the nanotube. Figure 24.22d shows the theoretical predictions for the dependence of the vibration frequency on gate voltage for a representative device. The predictions are based on finite-element (FE) analysis with the nanotube modeled as a long beam suspended over a trench. With the increase of the gap voltage, the deflection of the nanotube becomes larger and the stretching dominates the bending; therefore, the stiffness of the nanotube beam increases, and so does the resonance frequency. The theoretical predictions (Fig. 24.22d) show good qualitative agreement with experiments (Fig. 24.22b,c). The device showed a high force sensitivity (below 5 aN), which made it a small force transducer.

24.2.4.2 Nanowire Based NEMS Devices

Nanowires, like CNTs, are high-aspect-ratio one-dimensional nanostructures. The materials of nanowires include silicon [55,88–91], gold [92,93], silver [94–96], platinum [26], germanium [90,97–100], zinc oxide [101,102], and so on. Besides their size, the advantages offered by nanowires when employed in NEMS are their electronic properties, which can be controlled in a predictable manner during synthesis. This has not yet been achieved for CNTs. In contrast to CNTs, nanowires do not exhibit the same degree of flexibility, which may affect device fabrication and reliability. In the following section, two nanowire-based NEMS device are briefly reviewed.

24.2.4.2.1 Resonators

Figure 24.23 shows a suspended platinum nanowire resonator (Fig. 24.23a), reported by Husain et al. [26] in 2003, and the circuit used for magnetomotive drive and detection of its motion (Fig. 24.23b).

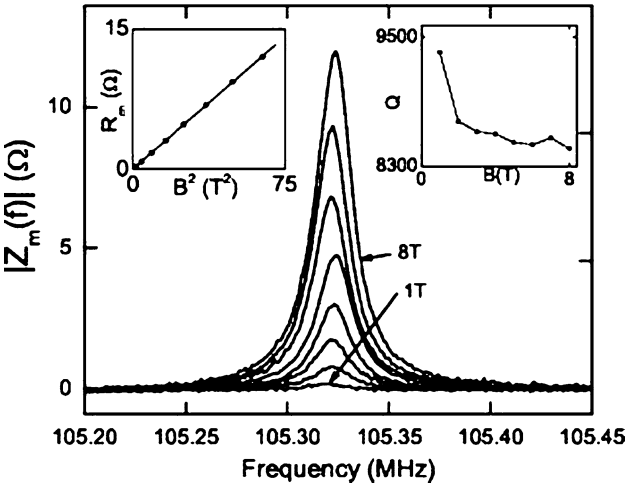

Fig. 24.24. Measured mechanical impedance of a Pt nanowire device as a function of frequency, at a series of magnetic fields from 1 to 8 T. *The left inset* shows the characteristic $\boldsymbol{B}^2$ dependence typical of magnetomotive detection. The *right inset* shows the quality factor Q as a function of magnetic field. (Reprinted with permission from Husain et al. [26] Copyright 2003, American Institute of Physics)

Synthesized platinum nanowires were deposited on a Si substrate capped by a 300-nm-thick layer of thermally grown silicon dioxide and prepatterned with Au alignment marks. The location of the deposited wires was mapped, by means of optical microscopy, using their strong light scattering properties [95,103]. Metallic leads (5 nm Cr, 50 nm Au) to individual wires were subsequently patterned by electron-beam lithography, evaporation, and lift-off. Finally, the SiO_2 was removed by wet etching (HF) to form suspended nanowire structures. The suspended Pt nanowire shown in Fig. 24.23a has a diameter of 43 nm and a length of 1.3 μm. A magnetomotive detection scheme (Fig. 24.23b), in which an AC drives a beam in a transverse magnetic field, was used to drive and read out the resonators. Figure 24.24 shows the measured motion-induced impedance of the nanowire device, $|Z_m(f)|$, versus frequency. The measured quality factor Q was approximately 8500 and decreased slightly with the increase in magnetic field. It was noted that the characteristic curve shown in Fig. 24.24 corresponds to a linear response of the beam. Badzey et al. [55] reported a doubly clamped nanomechanical Si beam working in the nonlinear response region. The nonlinear response of the beam displays notable hysteresis and bistability in the amplitude–frequency space when the frequency sweeps upward and downward. This particular behavior shows that the device can be used as mechanical memory elements.

24.2.4.2.2 Nanoelectromechanical Programmable Read-Only Memories

A nanowire-based nanoelectromechanical programmable read-only memory (NEMPROM) reported by Ziegler et al. [99] in 2004 is shown in Fig. 24.25a. The ger-

manium nanowire was synthesized directly onto a macroscopic gold wire (diameter 0.25 mm). The combination of a transmission electron microscope (TEM) and a STM was used to control and visualize the nanowire under investigation. Figure 24.25b–g illustrates how the device can work as a NEMPROM. In equilibrium, the attractive van der Waals force and electrostatic interactions between the nanowire and the gold electrode are countered by the elastic force from the deflection of the nanowire. Figure 24.25b shows the position of the nanowire with relatively low applied voltage. With the increase in voltage, the nanowire moves closer to the electrode (Fig. 24.25c). When the applied voltage exceeds a certain value, a jump-to-contact happens, i.e., the nanowire makes physical contact with the electrode (Fig. 24.25d). The nanowire remains in contact with the electrode even when the electrostatic field is removed because the van der Waals force is larger than the elastic force (Fig. 24.25e). This is the "on" state of the NEMPROM. The NEMPROM device can be switched off by mechanical motion or by heating the device above the stability limit to overcome the van der Waals attractive forces. Figure 24.25f and g shows the separation of the nanowire and the electrode after imposing a slight mechanical motion, resulting in a jump-off-contact event. This is the "off" state of the NEMPROM. The working principle of a NEMPROM is similar to that of a NRAM [1] since both of them employ van der Waals energy to achieve the bistability behavior, although the usage of germanium may provide better control of size and electrical behaviors of the device than that of CNT.

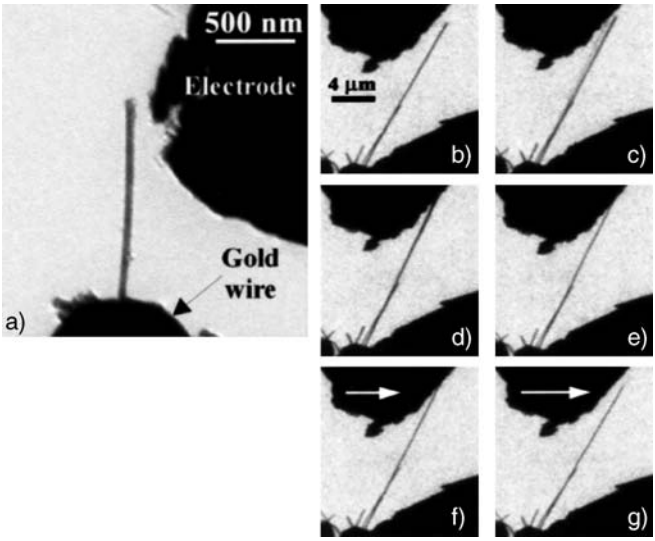

Fig. 24.25. (**a**) TEM image of a Ge nanowire device. (**b**)–(**d**) TEM sequence showing the jump-to-contact of a Ge nanowire as the voltage is increased. (**e**) TEM image demonstrating the stability of the device after removal of the electrostatic potential. (**f**),(**g**) TEM sequence demonstrating the resetting behavior of the device. (Reprinted with permission from Ziegler et al. [99] Copyright 2004, American Institute of Physics)

24.2.5 Future Challenges

NEMS offer unprecedented and intriguing properties in the fields of sensing and electronic computing. Although significant advancement has been achieved, there are many challenges that will need to be overcome before NEMS can replace and revolutionize current technologies. Among the issues that need further research and development are:

1. *Extremely high integration level*: For applications such as RAM and data storage, the density of the active components is definitely a key parameter. Direct growth and directed self-assembly are the two most promising methods to make NEMS devices with levels of integration orders of magnitudes higher than that of current microelectronics. A process for nanofabrication of the NEMS device developed by Ke and Espinosa [11], based on the directed self-assembly, is schematically shown in Fig. 24.26.
   a) A 1-μm-thick Si_3N_4 dielectric film is deposited on a Si wafer by low-pressure CVD. Then, a 50-nm-thick gold film (with 5-nm Cr film as the adhesion layer) is deposited by electron-beam evaporation and patterned by lithography to form the bottom electrodes. A 1-μm-thick SiO_2 layer is deposited by plasma-enhanced CVD (PECVD).
   b) The fountain-pen nanolithography technique [104] is then employed to functionalize specific areas, with widths down to 40 nm, either with polar chemical groups [such as the amino groups ($–NH_2$/$–NH_3^+$) of cysteamine] or carboxyl ($–COOH$/$–COO^-$) or with nonpolar groups [such as methyl ($–CH_3$)] from molecules like 1-octadecanethiol.
   c) The substrate is dipped into a solution containing prefunctionalized (with polar chemical groups) CNTs or nanowires, to adhere and self-assemble to the functionalized sites.
   d) The chip is patterned with electron-beam lithography and electron-beam evaporation of 100-nm gold film (lift-off, with 5-nm Cr film as the adhesion layer) to form the top electrodes.
   e) Removal of the SiO_2 layer using wet etching (HF) to free one end of the CNT cantilever completes the process.

The final product, a 2D array of NEMS devices with multiplexing capabilities, is schematically shown in Fig. 24.27. The top and bottom electrodes are interconnected to the pads, correspondingly. By applying voltage between the corresponding pads, the individual NEMS devices can be independently actuated.

2. *Better understanding the quality factor*: One of the keys to realizing the potential applications of NEMS is to achieve ultrahigh quality factors; however, it has been consistently observed that the quality factor of resonators decreases significantly with size scaling [7]. Defects in the bulk materials and interfaces, fabrication-induced surface damages, adsorbates on the surface, thermoelastic damping arising from inharmonic coupling between mechanical models and the phonon reservoir [105], and clamping losses [106] are a few commonly listed factors that can dampen the motion of resonators. Unfortunately, the dominant energy-dissipation mechanism in nanoscale mechanical resonators is still unclear.

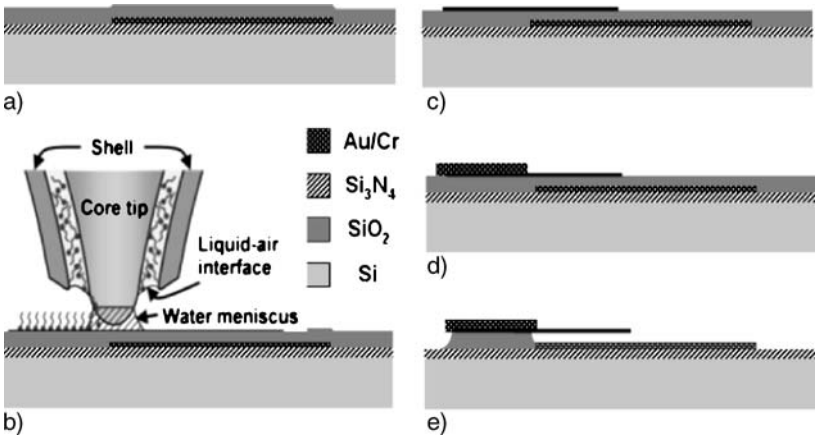

Fig. 24.26. The fabrication steps involving nanofountain probe functionalization

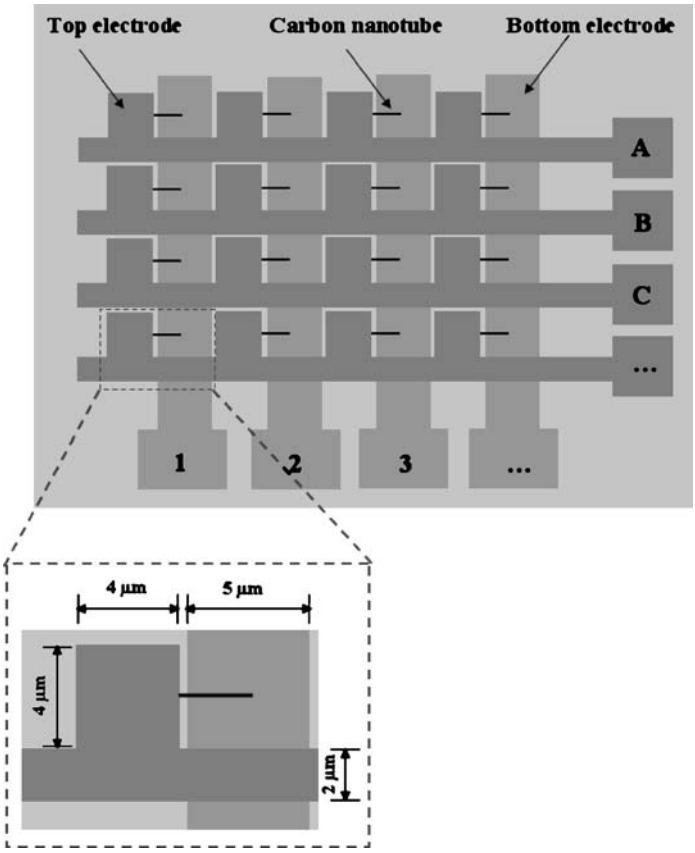

Fig. 24.27. Two-dimensional array of the NEMS device with multiplexing

3. *Reproducible and routine nanomanufacturing*: Fabrication reproducibility is key in applications such as mass sensors. Since the NEMS can respond to mass at the level of single atom or molecules, it places an extremely stringent requirement on the cleanness and precision of nanofabrication techniques. Likewise, devices that rely on van der Waals energy require dimensional control (e.g., gap dimension) on the order of a few nanometers.
4. *Quantum limit for mechanical devices*: The ultimate limit for NEMS is its operation at, or even beyond, the quantum limit [7]. In the quantum regime, the individual mechanical quanta are of the same order of magnitude as or greater than the thermal energy. Quantum theory should be utilized to understand and optimize force and displacement measurements. Recently, position resolution with a factor of 4.3 above the quantum limit was achieved for a single-electron transistor with high quality factor at millikelvin temperature [107]. The pursuit of NEMS devices operating at the quantum limit will potentially open new fields in science at the molecular level.

24.3 Modeling of NEMS

The design of NEMS depends on a thorough understanding of the mechanics of the devices themselves and the interactions between the devices and the external forces/fields. With the critical dimension shrinking from micron to nanometer scale, new physics emerges, so the theory typically applied to MEMS does not immediately translate to NEMS. For example, van der Waals forces from atomic interactions play an important role in NEMS, while they can be generally neglected in MEMS. The behavior of materials at the nanometer scale begins to be atomistic rather than continuous, giving rise to anomalous and often nonlinear effects, for example:

– The roles of surfaces and defects become more dominant.
– The devices become more compliant than continuum models predict.
– Molecular interactions and quantum effects become key issues, to the point that thermal fluctuation could make a major difference in the operation of NEMS.

For instance, the nanoresonators reported by the research groups of Roukes and Craighead are operated in the gigahertz range and usually have sizes within $200 \times 20 \times 10\,\mathrm{nm}^3$ [108]. Devices of this size and smaller are so miniscule that material defects and surface effects have a large impact on their performance.

In principle, atomic-scale simulations should reliably predict the behavior of NEMS devices; however, atomic simulations of the entire NEMS involve prohibitively expensive computational resources or exceed current computational power. Alternatively, multiscale modeling, which simulates the key region of a device with an atomistic model and other regions with a continuum model, can well serve the purpose under the circumstance of limited computational resources. Besides, it has been demonstrated that the behavior of some nanostructures, like CNTs, can be approximated by continuum mechanics models, based on the same potentials governing molecular dynamics (MD) simulation [109], if the surface nonideality of the nanostructures is neglected. Thus, continuum mechanics models are still adequate for the design of NEMS, in particular, in the initial stages.

24.3.1 Multiscale Modeling

Multiscale modeling is a technique to bridge the atomic simulations and continuum modeling. It generally makes use of coarse–fine decomposition in order to make computation more tractable. Atomistic simulation methods are typically used for the regions where individual MD information is crucial, where continuum modeling approaches are selected for all the other regions in which the deformation is considered to be homogeneous and smooth. In the atomistic domain, MD and quantum mechanics (QM) are typically employed, while in the continuum domain, the FE method (FEM) is often used. MD deals with the interaction of many thousands of atoms or more according to an interaction law. The "constitutive" behavior of each atom is governed by QM. QM involves the electronic structure, which in turn determines the interatomic force law – the "constitutive" behavior of each atom. However, in practice, the interatomic force laws have been determined empirically based on both QM and experiments. To model the response of NEMS devices, MD and continuum mechanics are generally adequate; hence, here we restrict our discussion to the basic ideas behind these two models. In some cases, QM modeling is required so the reader should consult the information on QM.

Multiscale modeling can be pursued sequentially (hierarchically) or concurrently. In the sequential method, information from each model at a given scale is passed to the next modeling level. In this fashion, "informed" or physically motivated models are developed at larger scales. Sequential techniques are based on the assumption of homogeneous lattice deformation; therefore, they are more effective for elastic single-phase problems. Challenges may arise from modeling defects in atomic lattices, dislocations, and failure phenomena [110]. In concurrent multiscale modeling, the system is split into primarily two domains: the atomistic domain and the continuum domain. These two scales are strongly dependent on each other through a smooth interscale coupling. Concurrent approaches are more relevant for studying complicated problems, such as inhomogeneous lattice deformation and fracture in multiphase macroscopic materials. Separation of the scales/domains and interscale coupling mechanism are two key issues for the concurrent techniques.

Recently, a new approach for the multiscale modeling, *multiscale boundary conditions* for MD simulations, was proposed by Karpov et al. [111] and Wagner et al. [112]. This technique does not involve the explicit continuum modeling; therefore, the issues of separating the scale and interscale coupling do not exist. The coarse grain behavior is taken into account on the fine/coarse grain interface at the atomistic level through the lattice impedance techniques. Multiscale boundary conditions are employed within concurrent coupling methods to represent atomistic behaviors in the continuum domain. That results in a smooth atomistic-continuum scale coupling, without involving a costly artificial handshake region which is typically mandatory for concurrent approaches. This approach can apply to multidimensional problems through the use of the Fourier analysis of periodic structures [113, 114].

As an example of sequential multiscale modeling, we discuss how the mechanical properties of bulk tantalum were calculated using a multiscale modeling strategy. Moriarty et al. [115] started with fundamental atomic properties and

used rigorous quantum-mechanical principles calculations to develop accurate interatomic force laws that were then applied to atomistic simulations involving many thousands of atoms. From these simulations, they derived the properties of individual dislocations in a perfect crystal and then, with a new microscale simulation technique, namely dislocation dynamics, examined the behavior of large collections of interacting dislocations at the microscale in a grain-sized crystal. They modeled the grain interactions in detail with FE simulation, and from those simulations, they finally constructed appropriate models of properties such as yield strength in a macroscopic volume of tantalum. At each length scale, the models were experimentally tested and validated with available data. The concept of information passing between models, from quantum modeling to atomic to continuum scale, is quite general and can be applied in a variety of problems, including NEMS.

24.3.1.1 Concurrent Multiscale Modeling

In a concurrent method, simulations at different length scales and time scales are performed simultaneously. The behavior at each scale depends strongly on the other. Atomistic approaches, such as MD, are used to describe behaviors of the materials in the atomistic regions, where characteristics of individual atoms are crucial, while continuum approaches, such as the FEM, are selected for the continuum domain, where the deformation is uniform and smooth.

MD computes the classical trajectories of atoms by integrating Newton's law, $F = ma$, for the system. In the MD domain, the interaction force follows an empirical potential. Consider a set of n_{M} molecules with the initial coordinates X_1, $I = 1$ to n_{M}. Let the displacements be denoted by $d_{\mathrm{I}}(t)$. The potential energy is then given by $W_{\mathrm{M}}(d)$. For a given potential function $W_{\mathrm{M}}(d)$, an equilibrium state is given by

$$dW_{\mathrm{M}}(d) = 0 \, . \tag{24.8}$$

From the continuum viewpoint, the governing equations arise from conservation of mass, momentum, and energy. Using a so-called total Lagrangian description [116], we can write the linear momentum equations as

$$\frac{\partial P_{ij}}{\partial X_j} + \rho_0 b_i = \rho_0 \ddot{u}_i \, , \tag{24.9}$$

where ρ_0 is the initial density, P the nominal stress tensor, b the body force per unit mass, u the displacement, and the superposed dots denote material time derivatives.

In the following section, we review some of the concurrent methods reported in the literature, including macroscopic, atomistic, and ab initio dynamics (MAAD), quasi-continuum method, scale bridging method, and coupling method, with the focus on the scale coupling mechanism and its application to the modeling of CNTs and microsystems/nanosystems. Reviews of the applications of these methods on modeling of other nanomaterials/nanostructures can be found in [110,117–119,151].

24.3.1.1.1 Macroscopic, Atomistic, and ab Initio Dynamics

MAAD is a length-scale concurrent coupling method developed by Abraham et al. [120, 121] and is named after the computation at three different length scales: macroscopic, atomistic, and ab initio dynamics. It is one of the early efforts to build a concurrent multiscale model. In this method, three different computational methods, namely tight-binding (TB), MD and FE are concurrently linked together. The dynamics of the entire targeted domain is governed by a total Hamiltonian function that combines the separate Hamiltonians of the three different scales, namely [121],

$$\begin{aligned} H_{\mathrm{Tot}} = {} & H_{\mathrm{FE}}(\{\boldsymbol{u}, \dot{\boldsymbol{u}}\} \in \mathrm{FE}) + H_{\mathrm{FE/MD}}(\{\boldsymbol{u}, \dot{\boldsymbol{u}}, \boldsymbol{r}, \dot{\boldsymbol{r}}\} \in \mathrm{FE/MD}) \\ & + H_{\mathrm{MD}}(\{\boldsymbol{r}, \dot{\boldsymbol{r}}\} \in \mathrm{MD}) + H_{\mathrm{MD/TB}}(\{\boldsymbol{r}, \dot{\boldsymbol{r}}\} \in \mathrm{MD/TB}) \\ & + H_{\mathrm{TB}}(\{\boldsymbol{r}, \dot{\boldsymbol{r}}\} \in \mathrm{TB}) \,, \end{aligned} \tag{24.10}$$

where, $\boldsymbol{r}$ and $\dot{\boldsymbol{r}}$ are the positions and the velocities of atoms in the TB and MD regions; $\boldsymbol{u}$ and $\dot{\boldsymbol{u}}$ are the displacements and time rate of change of elements in the FE region; MD/TB and FE/MD refer to the handshake regions. The equations of motion of all the variables are obtained by taking the appropriate derivative of H_{Tot} and, for a given set of initial conditions, the system evolves in a manner that conserves the total energy. More detailed information about the implementation of this technique can be found in [122].

This approach has been successfully applied to the investigation of crack propagation in a brittle solid, such as silicon [120], and microsystems/nanosystems, such as microresonators and microgears [108], as shown in Fig. 24.28. Figure 24.28a shows the schematic diagrams of domain decomposition for a microresonator. MD is used in the regions of the device with moderate strain oscillation while the FEM is used in the region where the change of strain is small. TB is used in regions of very large strain and bond breaking, such as at defects. These three length scales are smoothly coupled through the MD/FE and TB/MD handshaking. In brief, the MD/FE handshaking is accomplished through a mean force boundary condition. That is, the FE and MD regions overlap at the interface, and FE mesh nodes are positioned at the equilibrium positions of the corresponding MD atoms. The handshaking between the MD region and the TB region is accomplished through the termination of the chemical bonds that extend from the TB cluster. Various effects such as bond breaking, defects, internal strain, surface relaxation, statistical noise, and dissipation due to internal friction are included in the simulation.

The application of MAAD on modeling of microgears is illustrated in Fig. 24.28b. Such devices are presently made at the 100-μm scale and rotate at speeds of 150,000 rpm. The next generation of devices (nanogears), based on nanofabrication, are expected to be below the 1-μm level. The effects of wear, lubrication, and friction at the nanoscale are expected to have a significant consequence for the performance of the system; hence, the need for detailed modeling of these effects. The process of nanogear teeth grinding against each other cannot be simulated accurately with the FEM because deformation and bond breaking at the points of contact can only be treated empirically or with phenomenological models. Alter-

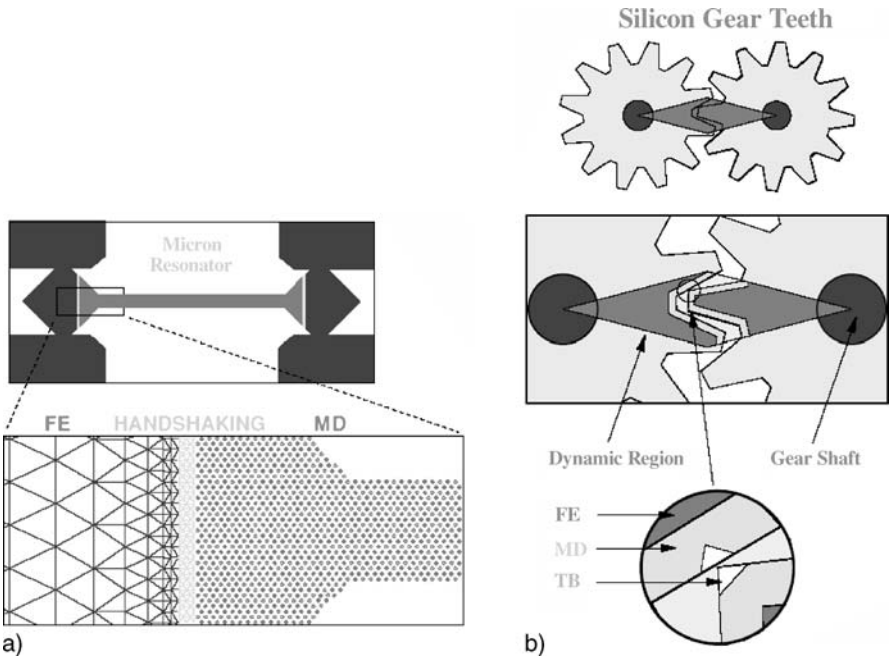

Fig. 24.28. (**a**) Scale decomposition for a microresontaor. Molecular dynamics (MD) is used in the regions of the device with moderate strain oscillators, while a finite-element (FE) method is used in the peripheral regions, where the change in strain is small. The two are joined through a consistent boundary condition in the handshake region, and both are run concurrently in lock-step. (**b**) Dynamic simulation zone and domain decomposition for coupling of length scales in microgears: from continuum (FE), to atomistic (MD) to electronic structure (tight-binding, TB). (Reprinted with permission from Rudd et al. [108] Copyright 1999, Applied Computational Research Society)

natively, multiscale modeling provides a good tool to predict chemomechanical-related issues for these devices, as shown in Fig. 24.28b. An inner region including the shaft is discretized by FEs. The handshaking between the FE and the MD region is accomplished by a self-consistent overlap region. In the gear–gear contact regions, in the nonlubricated case, a TB description is used as part of a QM simulation [108].

Two critical issues in this technique are the time step used in the simulation and the coupling of the different simulation domains. The time step used in the integration of the equations of motion (TB, MD, and FE) is determined by the time- step in the TB domain, which is the smallest and typically in the order of 10^{-15} s; therefore, many time steps are wasted in updating the MD and FE equations of motion, as the timescales governing those solutions are orders of magnitude larger. In MAAD, the coupling of the domains is accomplished by assuming in the transition region that each simulation contributes an equal amount of energy to the total energy. However, no rigorous studies have been performed to quantify the effectiveness of this method in eliminating spurious wave reflection at the simulation boundaries [110].

24.3.1.1.2 Quasi-continuum Method

The quasi-continuum method, originally developed by Tadmor et al. [123, 124], is a systematic computational approach that seeks a unified and efficient treatment of systems with a large number of atoms. It has been applied to the simulation of dislocation [123–126], grain boundary interactions [127, 128], nanoindentation [124, 128, 129], and fracture [130, 131]. In the quasi-continuum method, the continuum framework and continuum particle concept are retained, while the macroscopic constitutive equations are derived from atomistic interactions. The continuum particle is refined to the atomic level in critical regions such as near a defect and each continuum particle is considered as a small crystallite surrounding a representative atom. The quasi-continuum method has two different formulations: local and nonlocal. The local formulation of the quasi-continuum method is essentially the application of crystal elasticity by introducing a homogeneous deformation assumption. The advantage of this approach is that a large number of atoms can be lumped into a small set of representative atoms. The strain energy associated with the representative atoms can be computed by summing up the interatomic potential following the Cauchy–Born rule. A FE mesh is then imposed on top of the representative atoms. The deformation of the field variables can be approximated by the FE shape function and nodal values. The energy of the system can then be expressed in terms of the representative atoms, instead of all the atoms, with the approximate weights, resulting in significant computational savings. Hence, usage of the crystal elasticity approach, in the local formulation, allows the atoms in the system to be considered as a hyperelastic continuum material. The nonlocal formulation is introduced to allow atomic defects, e.g., dislocations, to occur when the FE approximation is insufficient to describe the deformation field. Some of the complications of this method include the following: (1) the mesh must be prescribed such that the nodes conform to the representative atoms at the interface; (2) the continuum mesh is required to be graded down to the scale of the atomic lattice in the region of the localized regions. A detailed review of the quasi-continuum and related methods can be found in [119].

24.3.1.1.3 Bridging Scale Method

The bridging scale method is a concurrent coupling method developed by Liu et al. [110–112, 132]. It assumes FE and MD solutions exist simultaneously in the entire computational domain and MD calculations are performed only in the region that is necessary; therefore, the issue of grading FE mesh down to lattice size as in quasi-continuum and MAAD methods does not arise here. The basic idea of the bridging scale method is to decompose the total displacement field $\boldsymbol{u}(\boldsymbol{x})$ into coarse and fine scales:

$$\boldsymbol{u}(\boldsymbol{x}, t) = \bar{\boldsymbol{u}}(\boldsymbol{x}, t) + \boldsymbol{u}'(\boldsymbol{x}, t) \ , \tag{24.11}$$

where $\bar{\boldsymbol{u}}(\boldsymbol{x}, t)$ is the coarse-scale solution and $\boldsymbol{u}'(\boldsymbol{x}, t)$ is the fine scale solution, corresponding to the part that has a vanishing projection onto the coarse-scale basic

function. The coarse-scale solution can be integrated by a basic FE shape function as $\bar{\boldsymbol{u}} = \boldsymbol{Nd}$, in which $\boldsymbol{d}$ is the FE solution and $\boldsymbol{N}$ is the shape function evaluated at atomic locations. The fine-scale solution can be obtained by $\boldsymbol{u}'(\boldsymbol{x}, t) = \boldsymbol{Qq}$ [133], where $\boldsymbol{q}$ is the MD solution and $\boldsymbol{Q} = \boldsymbol{I} - \boldsymbol{P}$, in which $\boldsymbol{P}$ is a projection operator that depends on both shape functions and the properties of the atomic lattice, and $\boldsymbol{I}$ is the identity operator.

One example in which the bridging scale method was employed successfully was the modeling of the buckling of a MWNT [134]. In the simulation, a 15-walled CNT with length of 90 nm was considered. The original MD system contained about 3×10^6 atoms. This was replaced with a system of 27,450 particles. In addition to

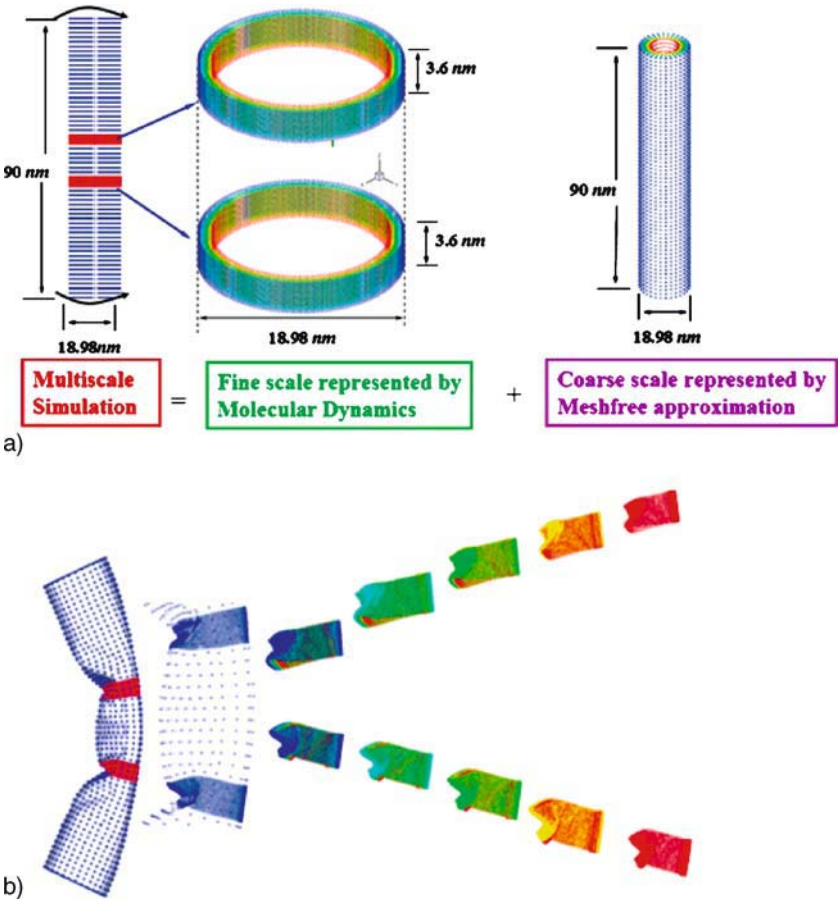

Fig. 24.29. Multiscale analysis of a 15-walled CNT by a bridging scale method. (**a**) The multiscale simulation model consists of ten rings of carbon atoms (with 49,400 atoms each) and a mesh-free continuum approximation of the 15-walled CNT by 27,450 nodes. (**b**) The global buckling pattern is captured by a mesh-free method, whereas the detailed local buckling of the ten rings of atoms is captured by a concurrent bridging scale MD simulation. (Reprinted with permission from Qian et al. [134] Copyright 2004, Elsevier)

the particles, two sections along the tube were enriched with molecular structures of MWNTs. The position of the enrichment was determined by a multiresolution analysis of the coarse-scale simulation. The multiscale configuration employed is illustrated in Fig. 24.29a. Figure 24.29b shows the buckling pattern at the final stage of loading and the energy density contour plot for each layer of the MWNT. Two distinctive buckling patterns can be seen, while the contour plot shows clearly the strain energy concentration at the buckling point. A unique feature revealed by the multiscale method is the details of the molecular structure at the kinks, which cannot be resolved by the coarse-scale representation alone. The atomic structures of the buckling region for each layer of the MWNT are plotted on the right-hand side of Fig. 24.29b.

The advantages of the bridging scale method over other concurrent methods are as follows: (1) no mesh gradation is required; (2) it does not involve calculation of any high-order tensors, such as the Piola–Kirchoff stress tensor, with associated gains in computational efficiency; (3) it can be extended to the dynamic regime [132, 133]. For these reasons, the bridging scale method has become a popular approach in the modeling of nanosystems.

24.3.1.1.4 Coupling Methods

Coupling methods are based on the coupling of continuum and molecular models through the definition of various domain decompositions [135]: (1) an edge-to-edge decomposition method, which has an interface between the two models, and (2) an overlapping-domain decomposition. A significant feature of the overlapping-domain decomposition method is that in the overlapping region, handshake region, the total potential energy is a linear combination of the continuum and atomistic potential energies.

An example of the overlapping-domain decomposition model is shown in Fig. 24.30. The complete domain in the initial configuration is denoted by Ω_0 and its boundaries by Γ_0. The domain is subdivided into the subdomains treated by

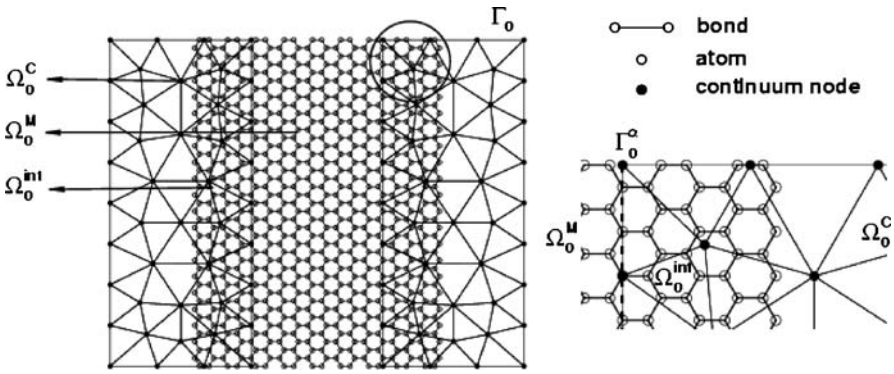

Fig. 24.30. Overlapping-domain decomposition method. (Reprinted with permission from Belytschko and Xiao [135]. Copyright 2003, Begell House)

continuum mechanics, Ω_0^{C}, and that treated by molecular mechanics, Ω_0^{M}, which is the domain encompassed by the atoms of the model. The intersection of these two domains is donated by Ω_0^{int} in the initial configuration and Ω^{int} in the current configuration (Ω^{int} is often called handshake domain). Γ_0^{α} denotes the edges of the continuum domain.

In the overlapping region Ω_0^{int}, the constraint imposed on the continuum model and molecular mechanics model is that the continuum displacements conform to the atomic displacements at the discrete position of the atoms, i.e.,

$$g_1 = ||\boldsymbol{u}(\boldsymbol{X}_{\mathrm{I}}) - \boldsymbol{d}_{\mathrm{I}}|| \ . \tag{24.12}$$

In the Lagrange multiplier method, the problem consists of finding the stationary condition of

$$W_{\mathrm{L}} = W^{\mathrm{int}} - W^{\mathrm{ext}} + \boldsymbol{\lambda}^{\mathrm{T}} g \ , \tag{24.13}$$

where W^{int} is the total internal potential of the system, W^{ext} is the total external potential energy, and $\boldsymbol{\lambda} = \{\boldsymbol{\lambda}_{\mathrm{I}}\}$ is the vector of Lagrange multipliers for the above constraint for each of the atoms.

The augmented Lagrangian method can be obtained by adding a penalty to (24.13), namely,

$$W_{\mathrm{AL}} = W^{\mathrm{int}} - W^{\mathrm{ext}} + \boldsymbol{\lambda}^{\mathrm{T}} g + \frac{1}{2} p \boldsymbol{g}^{\mathrm{T}} \boldsymbol{g} \ , \tag{24.14}$$

where p is the penalty parameter. If $p = 0$, (24.14) is identical to (24.13).

It is noted that the purpose of the handshake region is to assure a smoother coupling between the atomistic and continuum regions; therefore, an extremely fine FE mesh in the handshake region is required in order to provide adequate space resolution to match the positions of interface atoms and FEM nodal positions. At the front end of the continuum interface, the FEs have to be scaled down the chemical or ion bond lengths that may call forth costly inversions of large stiffness matrices [110]. As mentioned before, the recently proposed multiscale boundary conditions approach [112] may prove advantageous because it computes positions of actual next-to-interface atoms at the intrinsic atomistic level by means of a functional operator over the interface atomic displacements. This eliminates the need to have a costly handshake region at the atomic/continuum interface and a dense FEM mesh scale down to the chemical bond lengths.

In the edge-to-edge decomposition coupling method (Fig. 24.31), there are three types of particles. Besides the nodes of the continuum domain and the atoms of the molecular domain, virtual atoms are defined to model the bond angle-bending for bonds between the continuum and the molecular domains. The virtual atoms are connected with the molecular domain by virtual bonds.

The internal potential energy for the entire domain is given by the sum of continuum and molecular energies, viz.,

$$W^{\mathrm{int}} = W^{\mathrm{C}} + W^{\mathrm{M}} \ , \tag{24.15}$$

where W^{C} includes the stretching energy of virtual bonds and W^{M} includes the bond angle-bending potential resulting from the bond angle change between the

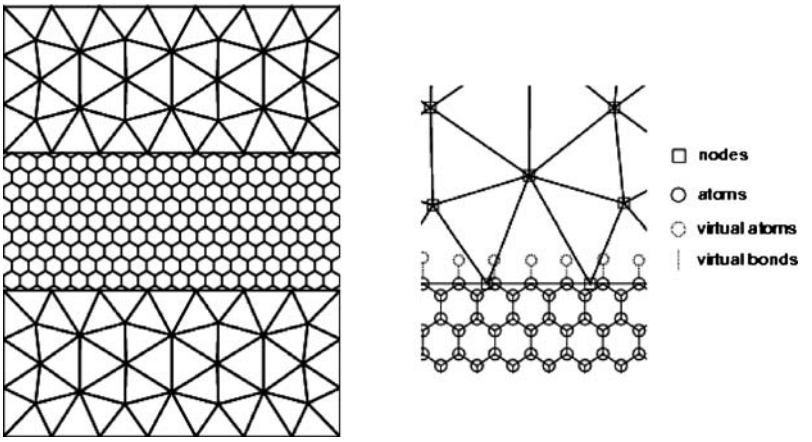

Fig. 24.31. Edge-to-edge coupling (*left*) and definition of particles and bonds in edge-to-edge coupling (*right*). (Reprinted with permission from Belytschko and Xiao [135]. Copyright 2003, Begell House)

virtual bonds and adjacent bonds in the molecular domain. The motion of each virtual atom will depend on the modes of the element that contain this virtual atom. The constraints given by (24.12) can then be imposed by means of the Lagrange multiplier method (24.13) or the augmented Lagrangian method (24.14).

An example illustrating the performance of these methods is shown in Fig. 24.32. The deformed configuration of a bent graphite sheet, with bending angle of 25°, was obtained using three different modeling techniques: (1) pure atomistic method, (2) overlapping-domain decomposition method, and (3) edge-to-edge decomposition method. A comparison of the predictions is shown in Fig. 24.32, which reveals that the deformation configurations are nearly identical. Figure 24.33 shows a comparison of predictions for the bending of a SWNT, with bending angle of 30°, using molecular mechanics (Fig. 24.33a) and overlapping coupling (Fig. 24.33b) methods. A comparison of the potential energies obtained by these two approaches is shown in Fig. 24.33c. The differences are small and likely due to the fact that the continuum model did not capture the tiny kinks predicted by the molecular mechanics model. Figure 24.34 shows another example of modeling the fracture of CNTs using the

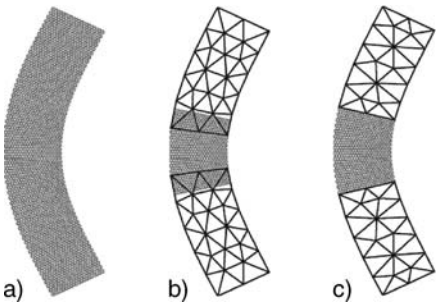

Fig. 24.32. Bending of graphite sheets. Comparison of deformed configurations obtained by means of (**a**) molecular mechanics, (**b**) overlapping coupling, and (**c**) edge-to-edge coupling. (Reprinted with permission from Belytschko and Xiao [135]. Copyright 2003, Begell House)

overlapping-coupling method. In the simulation, two nested nanotubes with van der Waals interactions between the shells were considered. The molecular model was used only in a small subdomain surrounding a defect, while the FE model was employed outside of the molecular model (Fig. 24.34). A modified Tersoff–Brenner

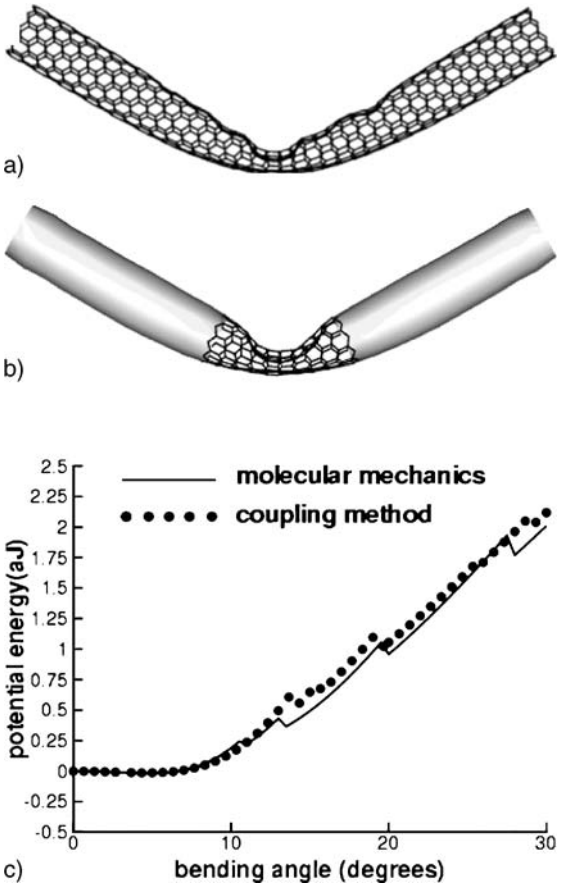

Fig. 24.33. Bending of a SWNT. Comparison of deformed configurations obtained by means of (**a**) molecular mechanics and (**b**) the overlapping-coupling method. (**c**) Comparison of potential energy as a function of bending angle. (Reprinted with permission from Belytschko and Xiao [135]. Copyright 2003, Begell House)

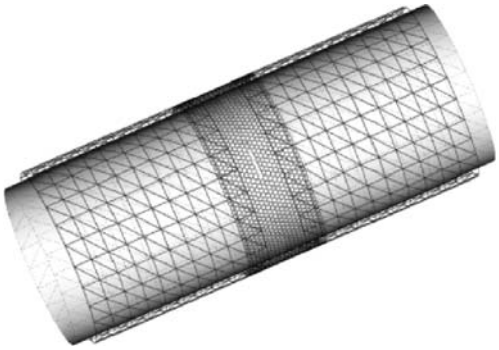

Fig. 24.34. CNT model for fracture study by the overlapping-coupling method. (Reprinted with permission from Belytschko and Xiao [135]. Copyright 2003, Begell House)

potential was employed to model the covalent C–C bond and the Lennard-Jones potential was employed to capture the intershell nonbonded (van der Waals) interactions. The load was only applied to the outer shell. The numerical results revealed that large vacancies are needed to explain the failure stresses experimentally measured in MWNTs. Furthermore, the simulations demonstrated that the van der Waals intershell interactions are negligible.

24.3.2 Continuum Mechanics Modeling

Many NEMS devices can be modeled either as biased cantilever beams or as fixed–fixed beams freestanding over a ground substrate, as shown in Fig. 24.35. The beams can be CNTs, nanowires, or small nanofabricated parts. The electromechanical characterization of NEMS involves the calculation of the elastic energy (E_{elas}), from the deformation of active components, the electrostatic energy (E_{elec}), and van der Waals energy (E_{vdW}) from atomic interactions. In the following we overview the continuum theory for each of these energy domains and derive the governing equations for both small and finite deformation regimes. We follow the work reported in [31, 109, 136–139].

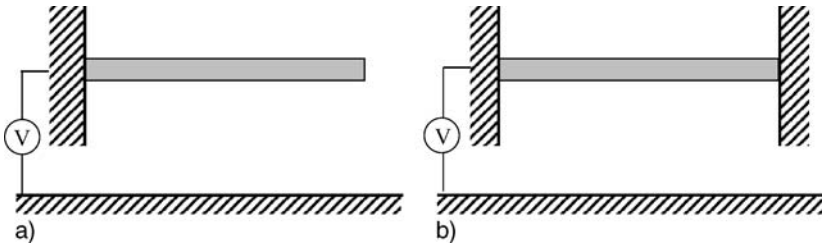

Fig. 24.35. NEMS devices: (**a**) Cantilever beam configuration; (**b**) doubly clamped beam configuration

24.3.2.1 Continuum Theory

24.3.2.1.1 Van der Waals Interactions

The van der Waals energy originates from the interaction between atoms. The Lennard-Jones potential is a suitable model to describe van der Waals interaction [140]. In the Lennard-Jones potential, there are two terms: one is repulsive and the other is attractive. The Lennard-Jones potential between two atoms i and j is given by

$$\phi_{ij} = \frac{C_{12}}{r_{ij}^{12}} - \frac{C_6}{r_{ij}^{6}} , \tag{24.16}$$

where r_{ij} is the distance between atoms i and j and C_6 and C_{12} are attractive and repulsive constants, respectively. For the carbon–carbon interaction, $C_6 = 15.2\,\text{eV}\,\text{Å}^6$ and $C_{12} = 24.1\,\text{keV}\,\text{Å}^{12}$ and the equilibrium spacing $r_0 = 3.414\,\text{Å}$ [141]. From (24.16), we can see that the repulsive components of the potential decay extremely fast and play an important role only when the distance is close to or smaller than r_0. The total van der Waals energy can be computed by a pairwise summation over all the atoms. The computational cost (number of operations) is proportional to the square of the number n of atoms in the system. For a NEMS device with millions of atoms, this technique is prohibitively expensive. Instead, a continuum model was established to compute the van der Waals energy by the double volume integral of the Lennard-Jones potential [142], i.e.,

$$E_{\text{vdW}} = \int_{\nu_1}\int_{\nu_2} n_1 n_2 \left(\frac{C_{12}}{r^{12}(\nu_1, \nu_2)} - \frac{C_6}{r^6(\nu_1, \nu_2)} \right) \mathrm{d}\nu_1\, \mathrm{d}\nu_2 \,, \tag{24.17}$$

where ν_1 and ν_2 represent the two domains of integration, and n_1 and n_2 are the densities of atoms for the domains ν_1 and ν_2, respectively. $r(\nu_1, \nu_2)$ is the distance between any point on ν_1 and ν_2.

Let us consider a SWNT freestanding above a ground plane consisting of layers of graphite sheets, with interlayer distance $d = 3.35$ Å, as illustrated in Fig. 24.36a. The energy per unit length of the nanotube is given by

$$\frac{E_{\text{vdw}}}{L} = 2\pi\sigma^2 R \sum_{n=1}^{N} \int_{-\pi}^{\pi} \left(\frac{C_{12}}{10[(n-1)d + r_{\text{init}} + R + R\sin\theta]^{10}} - \frac{C_6}{4[(n-1)d + r_{\text{init}} + R + R\sin\theta]^4} \right) \mathrm{d}\theta \,, \tag{24.18}$$

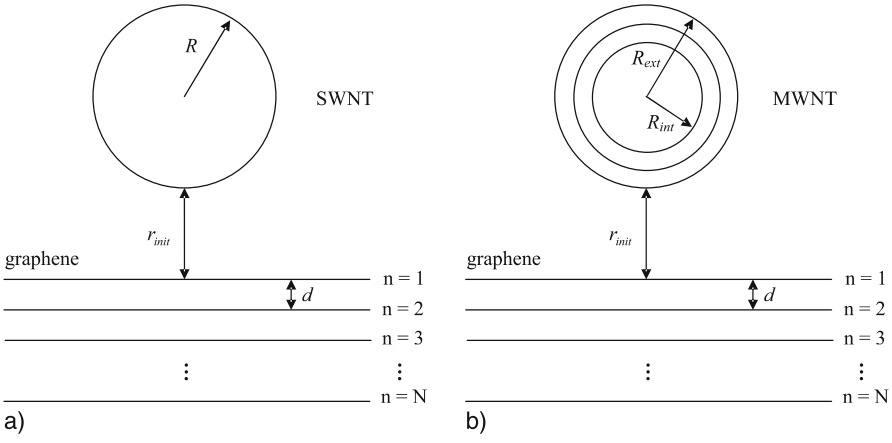

Fig. 24.36. Van der Waals integration of a SWNT (**a**) and a MWNT (**b**) over a graphite ground plane. (Reprinted with permission from Dequesnes et al. [109]. Copyright 2002, Institute of Physics)

where L is the length of the nanotube, R is the radius of the nanotube, r_{init} is the distance between the bottom of the nanotube and the top graphene sheet, N is the number of graphene sheets, and $\sigma \cong 38\,\text{nm}^{-2}$ is the graphene surface density. When r_{init} is much larger than the equilibrium spacing r_0, the repulsive component can be ignored and (24.18) can be simplified as [109]

$$\frac{E_{\text{vdW}}}{L} = C_6\sigma^2\pi^2 R \sum_{r=r_{\text{init}}}^{(N-1)d+r_{\text{init}}} \frac{(R+r)[3R^2+2(r+R)^2]}{2[(r+R)^2-R^2]^{7/2}} \,. \tag{24.19}$$

The accuracy of (24.19) in approximating the continuum van der Waals energy of a SWNT placed over a graphite plane is verified by the comparison with the direct pairwise summation of the Lennard-Jones potential given by (24.16) for a (16,0) tube, which is shown in Fig. 24.37 [109].

For a MWNT, as illustrated in Fig. 24.36b, the energy per unit length can be obtained by summing up the interaction between all separate shells and layers:

$$\frac{E_{\text{vdW}}}{L} = \sum_{R=R_{\text{int}}}^{R_{\text{ext}}} \sum_{r=r_{\text{init}}}^{(N-1)d+r_{\text{init}}} \frac{C_6\sigma^2\pi^2 R(R+r)[3R^2+2(r+R)^2]}{2[(r+R)^2-R^2]^{7/2}} \,, \tag{24.20}$$

where R_{int} and R_{ext} are the inner and outer radii of the nanotube, respectively.

The van der Waals force per unit length can be obtained as

$$q_{\text{vdw}} = \frac{\text{d}\left(\frac{E_{\text{vdw}}}{L}\right)}{\text{d}r} \,. \tag{24.21}$$

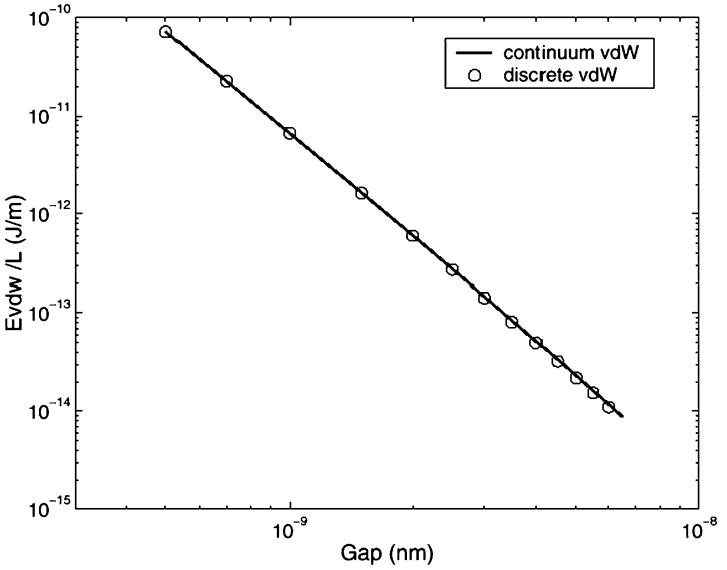

Fig. 24.37. Comparison of the continuum van der Waals energy given by (24.19) with the discrete pairwise summation given by (24.16). (Reprinted with permission from Dequesnes et al. [109]. Copyright 2002, Institute of Physics)

Thus, inserting (24.7) into (24.8) and taking the derivative with respect to r, one obtains [109]

$$q_{\mathrm{vdw}} = \sum_{R=R_{\mathrm{int}}}^{R_{\mathrm{ext}}} \sum_{r=r_{\mathrm{init}}}^{(N-1)d+r_{\mathrm{init}}} - \frac{C_6\sigma^2\pi^2 R\sqrt{r(r+2R)}(8r^4+32r^3R+72r^2R^2+80rR^3+35R^4)}{2[2r^5(r+2R)^5]^5} \tag{24.22}$$

24.3.2.1.2 Electrostatic Force

When a biased conductive nanotube is placed above a conductive substrate, there are induced electrostatic charges both on the tube and on the substrate. The electrostatic force acting on the tube can be calculated using a capacitance model [143].

Let us look at the electrostatic force for a conductive nanotube with finite length and round cross section, above an infinite ground plane. Although nanotubes have hollow structures, CNTs with capped ends are more electrochemically stable than those with open ends [144]; thus, nanotubes with finite length, as well as nanowires, can be geometrically approximated by conductive nanocylinders. For small-scale nanocylinders, the density of states on the surface is finite. The screening length, the distance that the "surface charge" actually penetrates into the cylinder interior, is found to be a nanometer-scale quantity [145]. For nanocylinders with transverse dimension, i.e., diameter, approaching the screening length, such as SWNTs, the finite size and density of states (quantum effects) have to be considered thoroughly when calculating the surface–volume charge distribution [146, 147]. For nanocylinders with transverse dimension much larger than the screening length, such as MWNTs or nanowires with large outer diameter, e.g., 20 nm, this quantum effect can be considered negligible. Thus, the charge distribution can be approximated by the charge distribution on a metallic, perfectly conductive cylinder with the same geometry, to which classical electrostatic analysis can be applied.

For infinitely long metallic cylinders, the capacitance per unit length is given by [143]

$$C_{\mathrm{d}}(r) = \frac{\pi\varepsilon}{a\cosh\left(1+\frac{r}{R}\right)}\,, \tag{24.23}$$

where r is the distance between the lower fiber of the nanocylinder and the substrate, R is the radius of the nanocylinder, and ε is the permittivity of the medium. For vacuum, $\varepsilon_0 = 8.854\times10^{-12}\,\mathrm{C^2\,N^{-1}\,m^{-2}}$. Equation (24.23) can be applied for infinitely long MWNTs with large diameters ($R = R_{\mathrm{ext}}$).

For the charge distribution on infinitely long SWNTs, Bulashevich and Rotkin [147] proposed a quantum correction, rendering the capacitance per unit length as

$$C = \frac{C_{\mathrm{d}}}{1+\frac{C_{\mathrm{d}}}{C_{\mathrm{Q}}}} \approx C_{\mathrm{d}}\left(1-\frac{C_{\mathrm{d}}}{C_{\mathrm{Q}}}\right)\,, \tag{24.24}$$

where $C_Q = e^2 \nu_m$, ν_M is the constant density of the states near the electroneutral level measured from the Fermi level.

For nanocylinders with finite length, there are two types of boundary surfaces – the cylindrical side surface and the planar end surface. Essentially classical distribution of charge density with a significant charge concentration at the cylinder end has been observed [146, 148, 149]. Here we discuss a model to calculate the electrostatic charge distribution on metallic cylindrical cantilevers based on a boundary element method, considering both the concentrated charge at the free end and the finite rotation due to the deflection of the cantilever [136].

Figure 24.38 shows the charge distribution along the length L of a freestanding nanotube, subjected to a bias voltage of 1 V. The contour plot shows the charge density (side view), while the curve shows the charge per unit length along the nanotube. The calculation was performed using the CFD-ACE+ software (a commercial code from CFD Research Corporation based on finite volume and boundary element methods). There is significant charge concentration on the free ends and uniform charge distribution in the center of the cantilever, which is found to follow (24.23). The charge distribution along a deflected cantilever nanotube is shown in Fig. 24.39. The parameters are $R_{ext} = 20\,\text{nm}$, $H = 500\,\text{nm}$, $L = 3\,\mu\text{m}$, and the gap between the free end and the substrate $r(L)$ is 236 nm. From Fig. 24.39, it is seen that, besides the concentrated charge on the free end, the clamped end imposes a significant effect on the charge distribution in the region close to it [145]; however, this effect can be considered negligible because its contribution to the deflection of the nanotube is quite limited. The charge distribution in regions other than the two ends closely follows (24.23). A formula for the charge distribution including end charge effects and the deflection of the cantilever is derived from a parametric analysis, as follows [136]:

$$C(r(x)) = C_d(r(x)) \left\{ 1 + 0.85[(H+R)^2 R]^{\frac{1}{3}} \delta(x - x_{tip}) \right\} = C_d(r(x))\{1 + f_c\}\,, \tag{24.25}$$

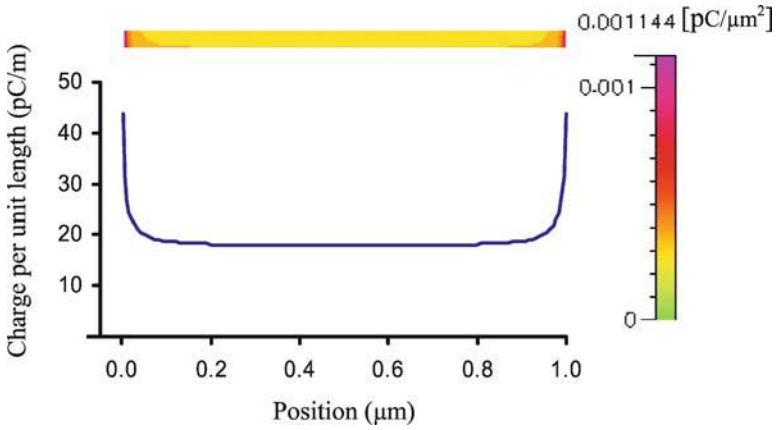

Fig. 24.38. Charge distribution for a biased nanotube. The device parameters are $R_{ext} = 9\,\text{nm}$, $H = 100\,\text{nm}$, and $L = 1\,\mu\text{m}$. (Reprinted with permission from Ke et al. [137]. Copyright 2005, The American Society of Mechanical Engineers)

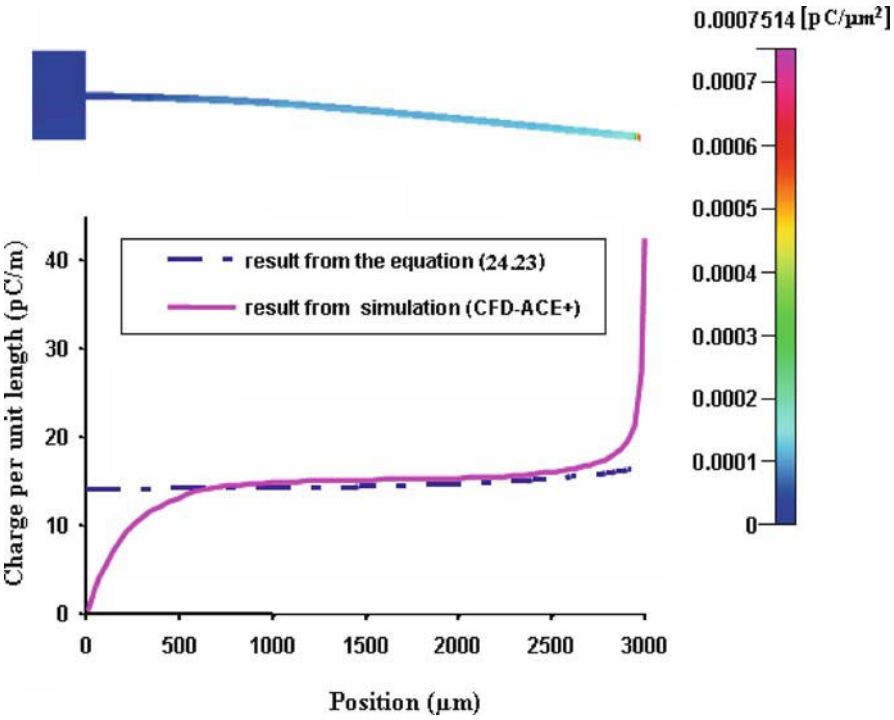

Fig. 24.39. *Top*: Two-dimensional side view of the charge distribution in a deflected nanotube cantilever. *Bottom*: Charge distribution per unit length along a deflected nanotube cantilever. The *solid line* is the simulation result performed with CFD-ACE+; the *dotted line* is plotted from (24.23). (Reprinted with permission from Ke and Espinosa [136]. Copyright 2005, The American Society of Mechanical Engineers)

where the first term in the bracket accounts for the uniform charge along the side surface of the tube and the second term, f_c, accounts for the concentrated charge at the end of the tube (for a doubly clamped tube, $f_c = 0$). H is the distance between the cantilever and the substrate when the cantilever is in a horizontal position, R is the radius of the tube (for a MWNT $R = R_{ext}$), $x = x_{tip} = L$ for small deflection (when considering the finite kinematics, i.e., large displacement, $x = x_{tip} \neq L$), $\delta(x)$ is the Dirac function, and $r(x) = H - w(x)$, with w being the tube deflection.

Thus, the electrostatic force per unit length of the nanotube is given by differentiation of the energy as follows [137]:

$$q_{elec} = \frac{1}{2}V^2\frac{dC}{dr} = \frac{1}{2}V^2\left(\frac{dC_d}{dr}\right)\{1 + f_c\}$$
$$= \frac{-\pi\varepsilon_0 V^2}{\sqrt{r(r+2R)}\, a\cosh^2\left(1+\frac{r}{R}\right)}(1 + f_c)\,, \tag{24.26}$$

where V is the bias voltage.

24.3.2.1.3 Elasticity

Continuum beam theory has been widely used to model the mechanics of nanotubes [28, 31, 109, 136, 138, 139]. The applicability and accuracy of the continuum theory have been evaluated by comparison with MD simulations [109]. Figure 24.40 shows the comparison of the deflection of a 20-nm-long, doubly clamped, double-walled nanotube with a diameter of 1.96 nm, calculated by MD simulation and by the beam equation, respectively. The solid black curve – the deflection predicated by the beam equation – follows closely the shape predicted by MD calculations.

Because nanotubes have high flexibility with strain at tensile failure on the order of 30% [150], nonlinear effects such as finite kinematics accounting for large displacement need to be considered in the modeling. This is particularly important for doubly clamped nanotube beams because the stretching from the finite kinematics stiffens the beam, resulting in a significant increase of the pull-in voltage, a key parameter in NEMS devices.

Fig. 24.40. Comparison between MD and beam theory for the deflection of a 20-nm-long fixed–fixed double-walled nanotube (diameter 1.96 nm). The *solid black curve* is the deflection predicated by beam theory. (Reprinted with permission from Dequesnes et al. [109]. Copyright 2002, Institute of Physics)

24.3.2.1.4 Governing Equations

The electromechanical characteristic of nanotube cantilevers or doubly clamped nanotube beams can be determined by coupling the van der Waals, electrostatic, and elastic forces. The governing equation under the small-deformation assumption (considering only bending) is given by [109]

$$EI\frac{\mathrm{d}^4 r}{\mathrm{d}x^4} = q_{\mathrm{elec}} + q_{\mathrm{vdw}} \ , \tag{24.27}$$

where r is the gap between the nanotube and the ground plane, x is the position along the tube, E is Young's modulus (for a CNT $E = 1$–1.2 TPa), I is the moment of inertia (for nanotubes $I = \frac{\pi}{4}(R_{\mathrm{ext}}^4 - R_{\mathrm{int}}^4)$, where R_{ext} and R_{int} are the outer and inner radii of the nanotubes, respectively), and q_{elec} and q_{vdw} are given by (24.26) and (24.22), respectively.

For cantilevers exhibiting large displacements, as shown in Fig. 24.41, the curvature of the deflection should be considered and the governing equation changes into [137]

$$EI\frac{\mathrm{d}^2}{\mathrm{d}x^2}\left(\frac{\frac{\mathrm{d}^2 r}{\mathrm{d}x^2}}{\left(1+\left(\frac{\mathrm{d}r}{\mathrm{d}x}\right)^2\right)^{\frac{3}{2}}}\right)=(q_{\mathrm{vdw}}+q_{\mathrm{elec}})\sqrt{1+\left(\frac{\mathrm{d}r}{\mathrm{d}x}\right)^2}\,. \tag{24.28}$$

For doubly clamped structures exhibiting finite kinematics, as shown in Fig. 24.42, stretching becomes significant as a consequence of the ropelike behavior of a doubly clamped nanotube. The corresponding governing equation is expressed as [137–139]

$$EI\frac{\mathrm{d}^4 r}{\mathrm{d}x^4}-\frac{EA}{2L}\int_0^L\left(\frac{\mathrm{d}r}{\mathrm{d}x}\right)^2\mathrm{d}x\frac{\mathrm{d}^2 r}{\mathrm{d}x^2}=q_{\mathrm{elec}}+q_{\mathrm{vdw}}\,, \tag{24.29}$$

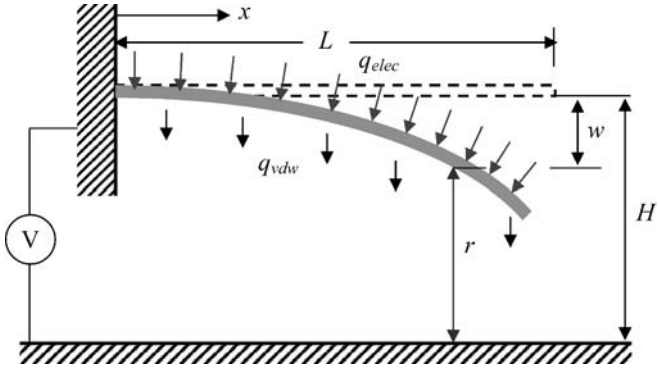

Fig. 24.41. Finite-kinematics configuration of a cantilever nanotube device subjected to electrostatic and van der Waals forces. (Reprinted with permission from Ke et al. [137]. Copyright 2005, The American Society of Mechanical Engineers)

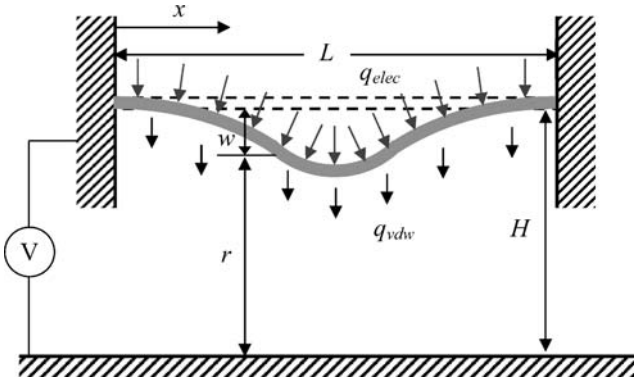

Fig. 24.42. Finite-kinematics configuration of a doubly clamped nanotube device subjected to electrostatic and van der Waals forces. (Reprinted with permission from Ke et al. [137]. Copyright 2005, The American Society of Mechanical Engineers)

where the term $\frac{EA}{2L}\int_0^L \left(\frac{\mathrm{d}r}{\mathrm{d}x}\right)^2 \mathrm{d}x$ is the tension along the axis of the tube due to stretching.

The aforementioned governing equations can be numerically solved by either direct integration or the finite-difference method.

24.3.2.2 Analytical Solutions

In this section, we discuss the analytical solutions of the electromechanical characteristic of the NEMS devices consisting of both cantilevered and doubly clamped nanotubes. In particular, the pull-in voltage calculations based on the energy method are reported [31, 138].

For nanotube cantilevers (singly clamped), the deflection of the cantilevered nanotube can be approximated by the following quadratic function [31]:

$$w(x) \approx \frac{x^2}{L^2} c \ , \tag{24.30}$$

where L is the length of the nanotube, c is a constant that represents the displacement of the end of the cantilever, and x is the coordinate along the nanotube.

The total energy of the system E_{total}, is expressed as

$$E_{\text{total}}(c) = E_{\text{elas}}(c) + E_{\text{elec}}(c) + E_{\text{vdW}}(c) \ , \tag{24.31}$$

where the elastic energy $E_{\text{elast}}(c)$, the electrostatic energy $E_{\text{elec}}(c)$, and van der Waals energy $E_{\text{vdW}}(c)$ can be obtained by integration as

$$E_{\text{elast}}(c) = \frac{EI}{2} \int_0^L \left(\frac{\mathrm{d}^2 w}{\mathrm{d}x^2}\right)^2 \mathrm{d}x \tag{24.32a}$$

and

$$E_{\text{elec,vdW}}(c) \approx \int_0^L \frac{\mathrm{d}E_{\text{elec,vdW}}(r(w(x)))}{\mathrm{d}x} \mathrm{d}x \ . \tag{24.32b}$$

The equilibrium condition is reached when the total energy reaches a minimum value, i.e.,

$$\frac{\mathrm{d}E_{\text{total}}}{\mathrm{d}c} = 0 \ . \tag{24.33a}$$

Similarly, the instability of the devices, i.e., pull-in, happens when the second-order derivative of the total energy equals zero, namely,

$$\frac{\mathrm{d}^2 E_{\text{total}}}{\mathrm{d}c} = 0 \ . \tag{24.33b}$$

The van der Waals interaction plays an important role only for a small gap between the nanotubes and substrate, i.e., a few nanometers; thus, it can be neglected in the analysis of NEMS with large gaps. We consider $E_{\text{vdw}} \approx 0$ in this analysis.

Under the assumption that the nanotube's (external) radius R_{ext} is much smaller than the distance r between the nanotube and ground plane, i.e., $R_{\text{ext}}/r \ll 1$, the pull-in voltage, considering the nonlinear finite kinematics and the concentrated charges at the free end, is given by [31]

$$V_{\underset{\text{PI}}{\text{S}}} \approx k_{\text{S}} \sqrt{\frac{1+K_{\text{S}}^{\text{FK}}}{1+K_{\text{S}}^{\text{TIP}}}} \frac{H}{L^2} \ln\left(\frac{2H}{R_{\text{ext}}}\right) \sqrt{\frac{EI}{\varepsilon_0}} \,, \tag{24.34a}$$

where

$$k_{\text{S}} \approx 0.85 \,, \quad K_{\text{S}}^{\text{FK}} \approx \frac{8H^2}{9L^2} \,, \quad K_{\text{S}}^{\text{TIP}} \approx \frac{2.55\left[R_{\text{ext}}(H+R_{\text{ext}})^2\right]^{\frac{1}{3}}}{L} \,, \tag{24.34b}$$

where subscripts S refer to singly clamped boundary conditions for cantilevers, superscript FK refers to finite kinematics, and superscript TIP refers to the charge concentration.

For doubly clamped nanotubes, the deflection is assumed to satisfy the boundary conditions $w(x=0,L) = w'(x=0,L) = 0$, namely, [138]

$$w(z) \approx 16\left[\left(\frac{x}{L}\right)^2 - 2\left(\frac{x}{L}\right)^3 + \left(\frac{x}{L}\right)^4\right] c \,, \tag{24.35}$$

where $w(x = L/2) = c$ is here an unknown constant that represents the displacement of the central point. The pull-in voltage can be expressed as [138]

$$V_{\underset{\text{PI}}{\text{D}}} = k_{\text{D}} \sqrt{1+k_{\text{D}}^{\text{FK}}} \, \frac{H+R}{L^2} \ln\left(\frac{2(H+R)}{R}\right) \sqrt{\frac{EI}{\varepsilon_0}} \,, \tag{24.36a}$$

where

$$k_{\text{D}} = \sqrt{\frac{1024}{5\pi S'(c_{\text{PI}})}\left(\frac{c_{\text{PI}}}{H+R}\right)} \,, \quad k_{\text{D}}^{\text{FK}} = \frac{128}{3003}\left(\frac{c_{\text{PI}}}{\rho}\right)^2 \,, \tag{24.36b}$$

where

$$\rho^2 = \frac{I}{A} = \frac{R_{\text{ext}}^2 + R_{\text{int}}^2}{4} \,, \quad S(c) = \sum_{i=1}^{\infty}\left(\frac{1}{\left(\ln\left(\frac{2(H+R)}{R}\right)\right)^i} \sum_{j=1}^{\infty} a_{ij}\left(\frac{c}{H+R}\right)^j\right) . \tag{24.36c}$$

Subscripts D refer to doubly clamped boundary conditions, c_{PI} is the central deflection of the nanotube at the pull-in, and the $\{a_{ij}\}$ in (24.36c) are known constants [138].

The accuracy of the analytical solutions is verified by the comparison with both numerical integration of the governing equations [137, 138] and experimental measurements (Sect. 24.3.2.3) [31]. The comparison between pull-in voltages evaluated

Table 24.1. Comparison between pull-in voltages evaluated numerically (num.) and theoretically (theo.) for doubly (D) and singly (S) clamped nanotube devices, respectively. $E = 1$ TPa, $R_{\text{int}} = 0$. For a cantilever nanotube device w denotes that the effect of charge concentration has been included. (Reprinted with permission from Ke et al. [137]. Copyright 2005, The American Society of Mechanical Engineers)

Case	BC	H (nm)	L (nm)	$R = R_{\text{ext}}$ (nm)	V_{PI} (V) (theo. linear)	V_{PI} (V) (num. linear)	V_{PI} (V) (theo. nonlinear)	V_{PI} (V) (num. nonlinear)
1	D	100	4000	10	3.20	3.18	9.06	9.54
2	D	100	3000	10	5.69	5.66	16.14	16.95
3	D	100	2000	10	12.81	12.73	36.31	38.14
4	D	150	3000	10	9.45	9.43	38.93	40.92
5	D	200	3000	10	13.53	13.52	73.50	77.09
6	D	100	3000	20	19.21	18.74	31.57	32.16
7	D	100	3000	30	38.57	37.72	51.96	50.63
8	S	100	500	10	27.28(w)	27.05(w)	27.52(w)	27.41(w)
9	S	100	500	10	27.28(w)	27.05(w)	30.87	31.66

numerically and theoretically for doubly and singly clamped nanotube devices is listed in Table 24.1 [137]. Columns six and seven in Table 24.1 compare analytical and numerical pull-in voltage predictions under the assumption of small deformations. Columns eight and nine in Table 24.1 compare analytical and numerical pull-in voltage predictions under the assumption of finite kinematics. The agreement is good (with a maximum discrepancy of 5%).

24.3.2.3 Comparison Between Analytical Predictions and Experiments

In this section, a comparison between analytical predictions and experimental data, for both small-deformation and finite-kinematics regimes, is presented.

24.3.2.3.1 Small-Deformation Regime

The nanotweezers experimental data reported by Akita et al. [9] in 2001, plotted in Fig. 24.43, is used to asses the model accuracy under small deformation. In this case, the nanotweezers are equivalent to a nanotube cantilever with length of 2.5 μm freestanding above an electrode with a gap of 390 nm. Symmetry is here exploited. In the same figure, a comparison between the analytically predicted nanotube cantilever deflection and the experimentally measured data is shown [31]. The analytical model includes the van der Waals force and charge concentration at the free end of the nanotube cantilever. Model parameters include Young's modulus, $E = 1$ TPa, external radius $R = R_{\text{ext}} = 5.8$ nm, and $R_{\text{int}} = 0$. The pull-in voltage from the analytical model is 2.34 V, while the experimentally measured pull-in voltage was 2.33 V. It is clear that the analytical prediction and experimental data for the deflection of the nanotube cantilever, as a function of applied voltage, are in very good agreement.

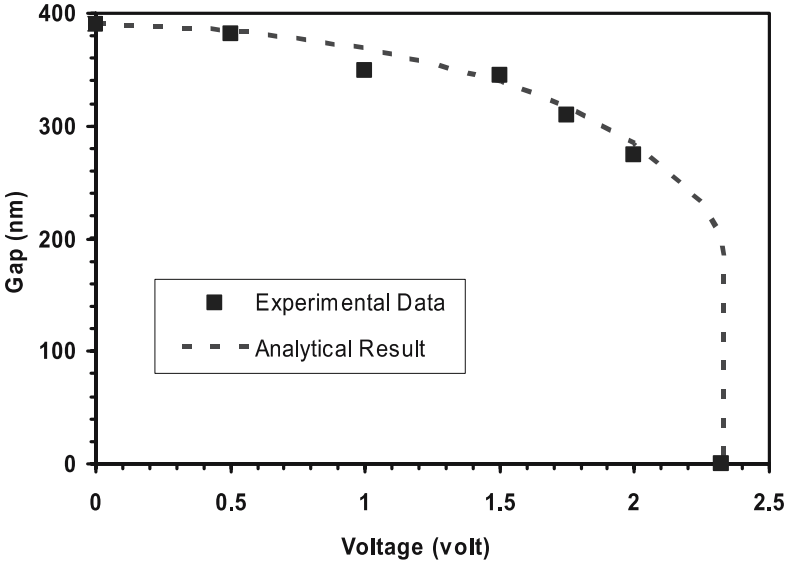

Fig. 24.43. Comparison between experimental data and theoretical prediction in the small-deformation regime. (Reprinted with permission from Ke at al. [31]. Copyright 2005, Elsevier)

24.3.2.3.2 Finite-Kinematics Regime

Experimental data corresponding to the deflection of CNT cantilevers in the finite-kinematics regime were recently obtained by in situ SEM measurements [31].

The configuration of the in situ measurement is shown in Fig. 24.44. The electrode was made of a silicon substrate coated with 50-nm Au film by electron-beam evaporation. This Si chip was attached onto the side of a Teflon block and mounted in the scanning electron microscope sample holder at an angle of 93° with respect to the holder plane. The nanotube cantilever fabricated by the method shown in Fig. 24.4 was placed horizontally and parallel to the electrode surface as schematically shown in Fig. 24.44. The distance between the top surface and the electron beam gun was 5 mm, while the distance between the nanotube and the electron-beam gun was measured to be 6.8 mm. Focusing on the electrode surface and adjusting the working distance to be 6.8 mm allowed a feature on the electrode, which was on the same horizontal plane as the nanotube, to be located. Such a feature is schematically marked as a line in Fig. 24.44. The horizontal distance between the nanotube and the line was controlled by the nanomanipulator and set to 3 μm. In the circuit, a resistor, $R_0 = 1.7\,\mathrm{M}\Omega$, was employed to limit the current. Because the ratio between the length of the nanotube and the gap between the nanotube and electrode is 2.3, the deflection of the nanotube can be considered to be in the finite-kinematics regime.

Figure 24.45 shows the SEM images of the deflection of the CNT as it is subject to increasing applied voltages. The feature on the electrode, which is in the same horizontal plane containing the cantilevered nanotube, is schematically marked as a solid black line in Fig. 24.45. These images clearly reveal changes in nanotube

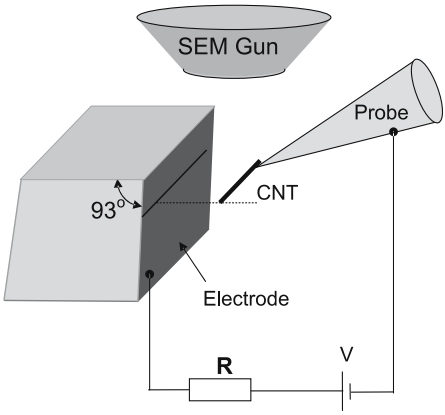

Fig. 24.44. The experimental configuration employed in the electrostatic actuation of MWNT. Reprinted with permission from Ke et al. [31]. (Copyright 2005, Elsevier, Ltd)

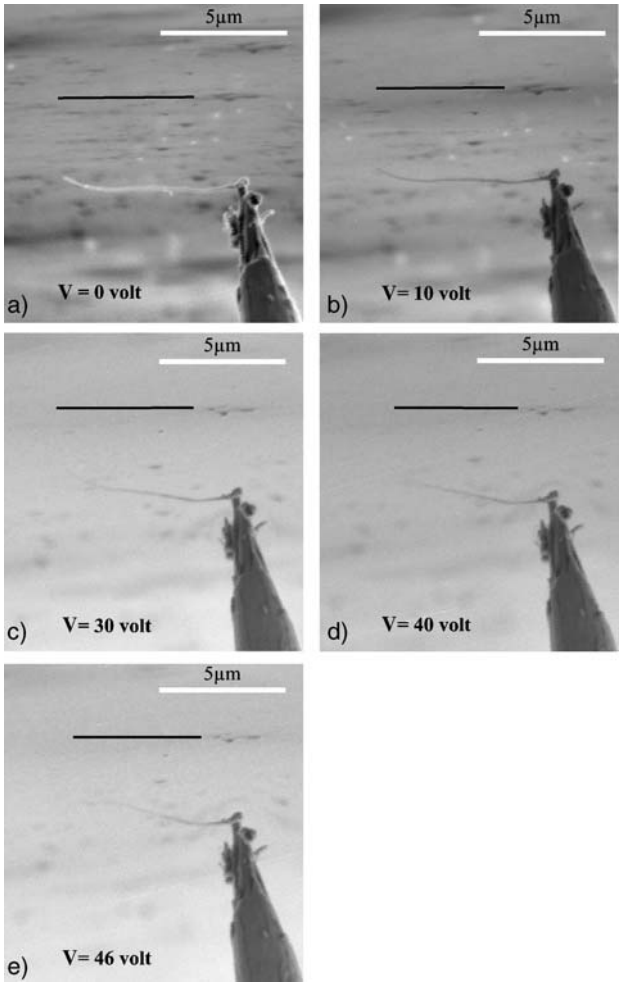

Fig. 24.45. SEM images of the deformed CNT at various bias voltages. (Reprinted with permission from Ke et al. [31]. Copyright 2005, Elsevier)

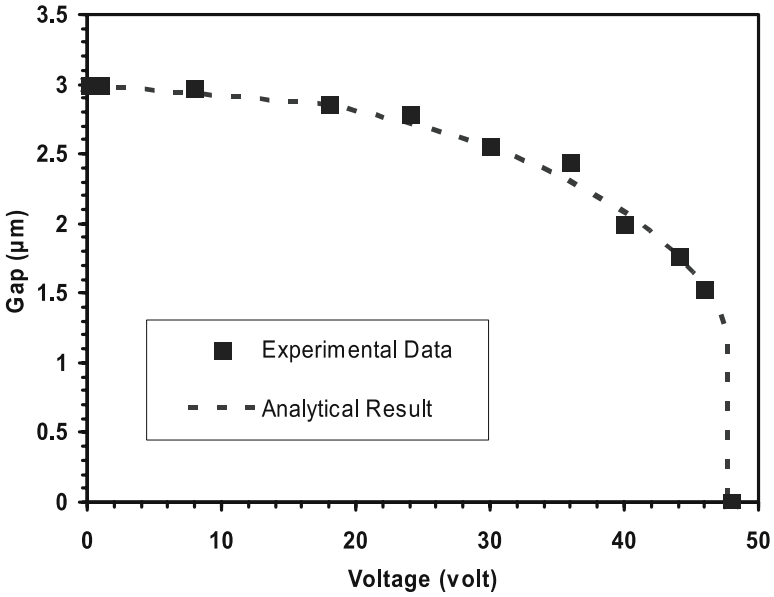

Fig. 24.46. Comparison between experimental data and theoretical prediction in the finite-kinematics regime. (Reprinted with permission from Ke et al. [31]. Copyright 2005, Elsevier)

deflection and local curvature as a function of applied voltage. A very noticeable effect, although difficult to quantify accurately, is the change in local curvature. The pull-in voltage, V_{PI}, was measured to be 48 V. Through digital image processing, the tip deflection as a function of voltage was measured.

The experimentally measured nanotube cantilever deflections, in the finite kinematics regime, are plotted in Fig. 24.46 [31]. The figure also shows a comparison between analytical prediction and experimental data. The analytical model includes finite kinematics, the van der Waals force, and charge concentration at the free end of the nanotube cantilever. For these predictions, the following parameters were employed: length of the nanotube, $L = 6.8\,\mu\mathrm{m}$, initial gap between nanotube and electrode, $H = 3\,\mu\mathrm{m}$, $R = R_{\mathrm{ext}} = 23.5\,\mathrm{nm}$, $R_{\mathrm{int}} = 0$, $E = 1\,\mathrm{TPa}$. The pull-in voltage given by the analytical analysis is 47.8 V, while the pull-in voltage measured experimentally was 48 V.

Acknowledgements. The authors acknowledge the support from the FAA through award no. DTFA03-01-C-00031 and the NSF through award no. CMS-0120866. We would like to express our appreciation to J. Newcomb and J. Larsen-Base for supporting this work. Work was also supported in part by the Nanoscale Science and Engineering Initiative of the NSF under NSF award no. EEC-0118025. Special thanks is due to E.G. Karpov, N. Pugno, and N. Moldovan for many useful discussions in relation to nanoscale modeling.

References

1. Rueckes T, Kim K, Joselevich E, Tseng GY, Cheung CL, Lieber CM (2000) Carbon nanotube-based nonvolatile random access memory for molecular computing, Science 289:94–97
2. Ekinci KL, Roukes ML (2005) Nanoelectromechanical systems. Review of Scientific Instruments 76:061101
3. Sazonova V, Yaish Y, Ustunel H, Roundy D, Arias TA, Mc Euen PL (2004) A tunable carbon nanotube electromechanical oscillator. Nature 431:284–287
4. Ilic B, Craighead HG, Krylov S, Senaratne W, Ober C, Neuzil P (2004) Attogram detection using nanoelectromechanical oscillators. Journal of Applied Physics 95:3694–3703
5. Davis ZJ, Abadal G, Kuhn O, Hansen O, Grey F, Boisen A (2000) Fabrication and characterization of nanoresonating devices for mass detection. Journal of Vacuum Science and Technology B 18:612–616
6. Roukes ML (1999) Yoctocalorimetry: phonon counting in nanostructures. Physica B 263:1–15
7. Roukes ML (2000) Nanoelectromechanical systems, presented at Technical Digest of the 2000 Solid-State Sensor and Actuator Workshop
8. Cleland AN, Roukes ML (1996) Fabrication of high frequency nanometer scale mechanical resonators from bulk Si crystals. Applied Physics Letters 69:2653–2655
9. Akita S, Nakayama Y, Mizooka S, Takano Y, Okawa T, Miyatake Y, Yamanaka S, Tsuji M, Nosaka T (2001) Nanotweezers consisting of carbon nanotubes operating in an atomic force microscope. Applied Physics Letters 79:1691–1693
10. Fennimore AM, Yuzvinsky TD, Han WQ, Fuhrer MS, Cumings J, Zettl A (2003) Rotational actuators based on carbon nanotubes. Nature 424:408–410
11. Ke CH, Espinosa HD (2004) Feedback controlled nanocantilever device. Applied Physics Letters 85:681–683
12. Kim P, Lieber CM (1999) Nanotube nanotweezers. Science 286:2148–2150
13. Kinaret JM, Nord T, Viefers S (2003) A carbon-nanotube-based nanorelay. Applied Physics Letters 82:1287–1289
14. Jang JE, Cha SN, Choi Y, Amaratunga GAJ, Kang DJ, Hasko DG, Jung JE, Kim JM (2005) Nanoelectromechanical switches with vertically aligned carbon nanotubes. Applied Physics Letters 87:163114
15. Iijima S (1991) Helical microtubules of graphitic carbon. Nature 354:56–58
16. Ajayan PM (1999) Nanotubes from carbon, Chemical Reviews 99:1787–1799
17. Ebbesen TW, Ajayan PM (1992) Large-scale synthesis of carbon nanotubes. Nature 358:220–222
18. Journet C, Maser WK, Bernier P, Loiseau A, delaChapelle ML, Lefrant S, Deniard P, Lee R, Fischer JE (1997) Large-scale production of single-walled carbon nanotubes by the electric-arc technique. Nature 388:756–758
19. Thess A, Lee R, Nikolaev P, Dai HJ, Petit P, Robert J, Xu CH, Lee YH, Kim SG, Rinzler AG, Colbert DT, Scuseria GE, Tomanek D, Fischer JE, Smalley RE (1996) Crystalline ropes of metallic carbon nanotubes. Science 273:483–487
20. Li WZ, Xie SS, Qian LX, Chang BH, Zou BS, Zhou WY, Zhao RA, Wang G (1996) Large-scale synthesis of aligned carbon nanotubes. Science 274:1701–1703
21. Qian D, Wagner GJ, Liu WK, Yu MF, Ruoff RS (2002) Mechanics of carbon nanotubes. Applied Mechanics Review 55:495–533
22. Mc Euen PL, Fuhrer MS, Park HK (2002) Single-walled carbon nanotube electronics. IEEE Transactions on Nanotechnology 1:78–85

23. Kuzumaki T, Mitsuda Y (2004) Dynamic measurement of electrical conductivity of carbon nanotubes during mechanical deformation by nanoprobe manipulation in transmission electron microscopy. Applied Physics Letters 85:1250–1252
24. Liu B, Jiang H, Johnson HT, Huang Y (2004) The influence of mechanical deformation on the electrical properties of single wall carbon nanotubes. Journal of the Mechanics and Physics of Solids 52:1–26
25. Tombler TW, Zhou CW, Alexseyev L, Kong J, Dai HJ, Lei L, Jayanthi CS, Tang MJ, Wu SY (2000) Reversible electromechanical characteristics of carbon nanotubes under local-probe manipulation. Nature 405:769–772
26. Husain A, Hone J, Postma HWC, Huang XMH, Drake T, Barbic M, Scherer A, Roukes ML (2003) Nanowire-based very-high-frequency electromechanical resonator Applied Physics Letters 83:1240–1242
27. Williams PA, Papadakis SJ, Patel AM, Falvo MR, Washburn S, Superfine R (2003) Fabrication of nanometer-scale mechanical devices incorporating individual multiwalled carbon nanotubes as torsional springs. Applied Physics Letters 82:805–807
28. Wong EW, Sheehan PE, Lieber CM (1997) Nanobeam mechanics: Elasticity, strength, and toughness of nanorods and nanotubes. Science 277:1971–1975
29. Falvo MR, Clary GJ, Taylor RM, Chi V, Brooks FP, Washburn S, Superfine R (1997) Bending and buckling of carbon nanotubes under large strain. Nature 389:582–584
30. Falvo MR, Taylor RM, Helser A, Chi V, Brooks FP, Washburn S, Superfine R (1999) Nanometre-scale rolling and sliding of carbon nanotubes. Nature 397:236–238
31. Ke CH, Pugno N, Peng B, Espinosa HD (2005) Experiments and modeling of carbon nanotube-based NEMS devices. Journal of the Mechanics and Physics of Solids 53:1314–1333
32. Taylor RMII, Superfine R (1999) Advanced Interfaces to Scanning Probe Microscopes, In: Nalwa HS (ed) Handbook of Nanostructured Materials and Nanotechnology 2. New York, Academic
33. Yu MF, Dyer MJ, Skidmore GD, Rohrs HW, Lu XK, Ausman KD, Von Ehr JR, Ruoff RS (1999) Three-dimensional manipulation of carbon nanotubes under a scanning electron microscope. Nanotechnology 10:244–252
34. Yu MF, Lourie O, Dyer MJ, Moloni K, Kelly TF, Ruoff RS (2000) Strength and breaking mechanism of multiwalled carbon nanotubes under tensile load. Science 287:637–640
35. Smith PA, Nordquist CD, Jackson TN, Mayer TS, Martin BR, Mbindyo J, Mallouk TE (2000) Electric-field assisted assembly and alignment of metallic nanowires. Applied Physics Letters 77:1399–1401
36. Chen XQ, Saito T, Yamada H, Matsushige K (2001) Aligning single-wall carbon nanotubes with an alternating-current electric field. Applied Physics Letters 78:3714–3716
37. Chung J, Lee J (2003) Nanoscale gap fabrication and integration of carbon nanotubes by micromachining. Sensors and Actuators A 104:229–235
38. Yamamoto K, Akita S, Nakayama Y (1998) Orientation and purification of carbon nanotubes using ac electrophoresis. Journal of Physics D: Applied Physics 31:L34–L36
39. Hughes MP, Morgan H (1998) Dielectrophoretic trapping of single sub-micrometre scale bioparticles. Journal of Physics D: Applied Physics 31:2205–2210
40. Ramos A, Morgan H, Green NG, Castellanos A (1998) Ac electrokinetics: a review of forces in microelectrode structures. Journal of Physics D: Applied Physics 31:2338–2353
41. Krupke R, Hennrich F, von Lohneysen H, Kappes MM (2003) Separation of metallic from semiconducting single-walled carbon nanotubes. Science 301:344–347
42. Lee SW, Lee DS, Morjan RE, Jhang SH, Sveningsson M, Nerushev OA, Park YW, Campbell EEB (2004) A three-terminal carbon nanorelay. Nano Letters 4:2027–2030
43. Huang Y, Duan XF, Wei QQ, Lieber CM (2001) Directed assembly of one-dimensional nanostructures into functional networks. Science 291:630–633

44. Fujiwara M, Oki E, Hamada M, Tanimoto Y, Mukouda I, Shimomura Y (2001) Magnetic orientation and magnetic properties of a single carbon nanotube. Journal of Physical Chemistry A 105:4383–4386
45. Huang SM, Dai LM, Mau AWH (1999) Patterned growth and contact transfer of well-aligned carbon nanotube films. Journal of Physical Chemistry B 103:4223–4227
46. Dai HJ (2000) Physics World 13:43
47. Kong J, Soh HT, Cassell AM, Quate CF, Dai HJ (1998) Synthesis of individual single-walled carbon nanotubes on patterned silicon wafers Nature 395:878–881
48. Zhang YG, Chang AL, Cao J, Wang Q, Kim W, Li YM, Morris N, Yenilmez E, Kong J, Dai HJ (2001) Electric-field-directed growth of aligned single-walled carbon nanotubes. Applied Physics Letters 79:3155–3157
49. Dai HJ (2002) Accounts of Chemical Research 35:1035
50. Nojeh A, Ural A, Pease RF, Dai HJ (2004) Electric-field-directed growth of carbon nanotubes in two dimensions. Journal of Vacuum Science and Technology B 22:3421–3425
51. Rao SG, Huang L, Setyawan W, Hong SH (2003) Large-scale assembly of carbon nanotubes. Nature 425:36–37
52. Piner RD, Zhu J, Xu F, Hong SH, Mirkin CA (1999) Dip-pen nanolithography. Science 283:661–663
53. Roukes ML (2001) Nanoelectromechanical systems face the future, Physics World 14:25–31
54. Ekinci KL (2005) Electromechanical transducers at the nanoscale: Actuation and sensing of motion in nanoelectromechanical systems (NEMS). Small 1:786–797
55. Badzey RL, Zolfagharkhani G, Gaidarzhy A, Mohanty P (2004) A controllable nanomechanical memory element. Applied Physics Letters 85:3587–3589
56. Craighead HG (2000) Nanoelectromechanical systems. Science 290:1532–1535
57. Zhu Y, Moldovan N, Espinosa HD (2005) A microelectromechanical load sensor for in situ electron and X-ray microscopy tensile testing of nanostructures. Applied Physics Letters 86:013506
58. Zalalutdinov M, Ilic B, Czaplewski D, Zehnder A, Craighead HG, Parpia JM (2000) Frequency-tunable micromechanical oscillator. Applied Physics Letters 77:3287–3289
59. Huang XMH, Zorman CA, Mehregany M, Roukes ML (2003) Nanodevice motion at microwave frequencies. Nature 421:496–496
60. Poncharal P, Wang ZL, Ugarte D, De Heer WA (1999) Electrostatic deflections and electromechanical resonances of carbon nanotubes. Science 283:1513–1516
61. Treacy MMJ, Ebbesen TW, Gibson JM (1996) Exceptionally high Young's modulus observed for individual carbon nanotubes. Nature 381:678–680
62. Greywall DS, Yurke B, Busch PA, Pargellis AN, Willett RL (1994) Evading amplifier noise in nonlinear oscillators. Physical Review Letters 72:2992–2995
63. Cleland AN, Roukes ML (1999) External control of dissipation in a nanometer-scale radiofrequency mechanical resonator. Sensors and Actuators A 72:256–261
64. Ekinci KL, Yang YT, Roukes ML (2004) Ultimate limits to inertial mass sensing based upon nanoelectromechanical systems. Journal of Applied Physics 95:2682–2689
65. Mohanty P, Harrington DA, Ekinci KL, Yang YT, Murphy MJ, Roukes ML (2002) Intrinsic dissipation in high-frequency micromechanical resonators. Physical Review B 66:085416
66. Dresselhaus MS, Dresselaus G, Avouris P (2001) Carbon Nanotubes. Berlin, Heidelberg, New York, Springer
67. Carr DW, Evoy S, Sekaric L, Craighead HG, Parpia JM (2000) Parametric amplification in a torsional microresonator. Applied Physics Letters 77:1545–1547
68. Carr DW, Sekaric L, Craighead HG (1998) Measurement of nanomechanical resonant structures in single-crystal silicon. Journal of Vacuum Science and Technology B 16:3821–3824

69. Meyer C, Lorenz H, Karrai K (2003) Optical detection of quasi-static actuation of nanoelectromechanical systems. Applied Physics Letters 83:2420–2422
70. Keeler BEN, Carr DW, Sullivan JP, Friedmann TA, Wendt JR (2004) Experimental demonstration of a laterally deformable optical nanoelectromechanical system grating transducer. Optics Letters 29:1182–1184
71. Kouh T, Karabacak D, Kim DH, Ekinci KL (2005) Diffraction effects in optical interferometric displacement detection in nanoelectromechanical systems. Applied Physics Letters 86:013106
72. Bocko MF, Stephenson KA, Koch RH (1988) Vacuum tunneling probe – a nonreciprocal, reduced-back-action transducer. Physical Review Letters 61:726–729
73. Presilla C, Onofrio R, Bocko MF (1992) Uncertainty-principle noise in vacuum-tunneling transducers. Physical Review B 45:3735–3743
74. Nunes G, Freeman MR (1993) Picosecond resolution in scanning-tunneling-microscopy. Science 262:1029–1032
75. Kanda Y (1982) A graphical representation of the piezoresistive coefficients in silicon. IEEE Transactions on Electron Devices 29:64–70
76. Hjort K, Soderkvist J, Schweitz JA (1994) Gallium-Arsenide as a Mechanical Material. Journal of Micromechanics and Microengineering 4:1–13
77. Bargatin I, Myers EB, Arlett J, Gudlewski B, Roukes ML (2005) Sensitive detection of nanomechanical motion using piezoresistive signal downmixing. Applied Physics Letters 86:133109
78. Dai HJ, Hafner JH, Rinzler AG, Colbert DT, Smalley RE (1996) Nanotubes as nanoprobes in scanning probe microscopy. Nature 384:147–150
79. Wong SS, Joselevich E, Woolley AT, Cheung CL, Lieber CM (1998) Covalently functionalized nanotubes as nanometre-sized probes in chemistry and biology. Nature 394:52–55
80. Jonsson LM, Axelsson S, Nord T, Viefers S, Kinaret JM (2004) High frequency properties of a CNT-based nanorelay. Nanotechnology 15:1497–1502
81. Ke CH, Espinosa HD (2006) In-situ electron microscopy electro-mechanical characterization of a NEMS bistable device, Small, (in press)
82. Ke CH (2006) Development of a Feedback Controlled Carbon Nanotube-Based Nanoelectromechanical Device. PhD dissertation, Northwestern University
83. Zapol P, Sternberg M, Curtiss LA, Frauenheim T, Gruen DM (2002) Tight-binding molecular-dynamics simulation of impurities in ultrananocrystalline diamond grain boundaries. Physical Review B 65:045403
84. Sternberg M, Curtiss LA, Gruen DM, Kedziora G, Horner DA, Redfern PC, Zapol P (2006) Carbon ad-dimer defects in carbon nanotubes. Physical Review Letters 96:075506
85. Tans SJ, Verschueren ARM, Dekker C (1998) Room-temperature transistor based on a single carbon nanotube. Nature 393:49–52
86. Zhou CW, Kong J, Dai HJ (2000) Intrinsic electrical properties of individual single-walled carbon nanotubes with small band gaps. Physical Review Letters 84:5604–5607
87. Minot ED, Yaish Y, Sazonova V, Mc Euen PL (2004) Determination of electron orbital magnetic moments in carbon nanotubes. Nature 428:536–539
88. Hu JT, Min OY, Yang PD, Lieber CM (1999) Controlled growth and electrical properties of heterojunctions of carbon nanotubes and silicon nanowires. Nature 399:48–51
89. Hu JT, Odom TW, Lieber CM (1999) Chemistry and physics in one dimension: Synthesis and properties of nanowires and nanotubes. Accounts of Chemical Research 32:435–445
90. Morales AM, Lieber CM (1998) A laser ablation method for the synthesis of crystalline semiconductor nanowires. Science 279:208–211
91. Yu DP, Lee CS, Bello I, Sun XS, Tang YH, Zhou GW, Bai ZG, Zhang Z, Feng SQ (1998) Synthesis of nano-scale silicon wires by excimer laser ablation at high temperature. Solid State Communications 105:403–407

92. Ji CX, Searson PC (2002) Fabrication of nanoporous gold nanowires. Applied Physics Letters 81:4437–4439
93. Wong TC, Li CP, Zhang RQ, Lee ST (2004) Gold nanowires from silicon nanowire templates. Applied Physics Letters 84:407–409
94. Bhattacharyya S, Saha SK, Chakravorty D (2000) Silver nanowires grown in the pores of a silica gel. Applied Physics Letters 77:3770–3772
95. Barbic M, Mock JJ, Smith DR, Schultz S (2002) Single crystal silver nanowires prepared by the metal amplification method. Journal of Applied Physics 91:9341–9345
96. Malandrino G, Finocchiaro ST, Fragala IL (2004) Silver nanowires by a sonoself-reduction template process. Journal of Materials Chemistry 14:2726–2728
97. Heath JR, Legoues FK (1993) A liquid solution synthesis of single-crystal germanium quantum wires. Chemical Physics Letters 208:263–268
98. Greytak AB, Lauhon LJ, Gudiksen MS, Lieber CM (2004) Growth and transport properties of complementary germanium nanowire field-effect transistors. Applied Physics Letters 84:4176–4178
99. Ziegler KJ, Lyons DM, Holmes JD, Erts D, Polyakov B, Olin H, Svensson K, Olsson E (2004) Bistable nanoelectromechanical devices. Applied Physics Letters 84:4074–4076
100. Wu YY, Yang PD (2000) Germanium nanowire growth via simple vapor transport. Chemistry of Materials 12:605–607
101. Banerjee D, Lao JY, Wang DZ, Huang JY, Ren ZF, Steeves D, Kimball B, Sennett M (2003) Large-quantity free-standing ZnO nanowires. Applied Physics Letters 83:2061–2063
102. Dai Y, Zhang Y, Bai YQ, Wang ZL (2003) Bicrystalline zinc oxide nanowires. Chemical Physics Letters 375:96–101
103. Mock JJ, Oldenburg SJ, Smith DR, Schultz DA, Schultz S (2002) Composite plasmon resonant nanowires. Nano Letters 2:465–469
104. Kim KH, Moldovan N, Espinosa HD (2005) A nanofountain probe with sub-100 nm molecular writing resolution. Small 1:632–635
105. Lifshitz R, Roukes ML (2000) Thermoelastic damping in micro- and nanomechanical systems. Physical Review B 61:5600–5609
106. Huang XMH, Prakash MK, Zorman CA, Mehregany M, Roukes ML (2003) Free-free beam silicon carbide nanomechanical resonators, presented at TRANSDUCERS '03 Proceedings of the 12th International Conference on Solid State Sensors. Actuators and Microsystems, Boston
107. La Haye MD, Buu O, Camarota B, Schwab KC (2004) Approaching the quantum limit of a nanomechanical resonator. Science 304:74–77
108. Rudd RE, Broughton JQ (1999) Journal of Modeling and Simulation of Microsystems 1:29
109. Dequesnes M, Rotkin SV, Aluru NR (2002) Calculation of pull-in voltages for carbon-nanotube-based nanoelectromechanical switches. Nanotechnology 13:120–131
110. Liu WK, Karpov EG, Zhang S, Park HS (2004) An introduction to computational nanomechanics and materials. Computer Methods in Applied Mechanics and Engineering 193:1529–1578
111. Karpov EG, Wagner GJ, Liu WK (2005) A Green's function approach to deriving non-reflecting boundary conditions in molecular dynamics simulations. International Journal for Numerical Methods in Engineering 62:1250–1262
112. Wagner GJ, Karpov EG, Liu WK (2004) Molecular dynamics boundary conditions for regular crystal lattices. Computer Methods in Applied Mechanics and Engineering 193: 1579–1601
113. Karpov EG, Stephen NG, Dorofeev DL (2002) On static analysis of finite repetitive structures by discrete Fourier transform. International Journal of Solids and Structures 39:4291–4310

114. Karpov EG, Stephen NG, Liu WK (2003) Initial tension in randomly disordered periodic lattices. International Journal of Solids and Structures 40:5371–5388
115. Moriarty JA, Belak JF, Rudd RE, Soderlind P, Streitz FH, Yang LH (2002) Quantum-based atomistic simulation of materials properties in transition metals. Journal of Physics: Condensed Matter 14:2825–2857
116. Belytschko T, Liu WK, Moran B (2000) Nonlinear Finite Elements for Continua and Structures. New York, Wiley
117. Curtin WA, Miller RE (2003) Atomistic/continuum coupling in computational materials science. Modelling and Simulation in Materials Science and Engineering 11:R33–R68
118. Vvedensky DD (2004) Multiscale modeling of nanostructures. Journal of Physics: Condensed Matter 16:1537–1576
119. Miller RE, Tadmor EB (2002) The quasicontinuum method: Overview, applications and current directions. Journal of Computer-Aided Materials Design 9:203–239
120. Abraham FF, Broughton JQ, Bernstein N, Kaxiras E (1998) Spanning the continuum to quantum length scales in a dynamic simulation of brittle fracture. Europhysics Letters 44:783–787
121. Broughton JQ, Abraham FF, Bernstein N, Kaxiras E (1999) Concurrent coupling of length scales: Methodology and application. Physical Review B 60:2391–2403
122. Rudd RE, Broughton JQ (2000) Concurrent coupling of length scales in solid state systems. Physica Status Solidi B 217:251–291
123. Tadmor EB, Ortiz M, Phillips R (1996) Quasicontinuum analysis of defects in solids. Philosophical Magazine A 73:1529–1563
124. Tadmor EB, Phillips R, Ortiz M (1996) Mixed atomistic and continuum models of deformation in solids. Langmuir 12:4529–4534
125. Rodney D, Phillips R (1999) Structure and strength of dislocation junctions: An atomic level analysis, Physical Review Letters 82:1704–1707
126. Shin CS, Fivel MC, Rodney D, Phillips R, Shenoy VB, Dupuy L (2001) Formation and strength of dislocation junctions in FCC metals: A study by dislocation dynamics and atomistic simulations. Journal De Physique IV 11:19–26
127. Shenoy VB, Miller R, Tadmor EB, Phillips R, Ortiz M (1998) Quasicontinuum models of interfacial structure and deformation. Physical Review Letters 80:742–745
128. Shenoy VB, Miller R, Tadmor EB, Rodney D, Phillips R, Ortiz M (1999) An adaptive finite element approach to atomic-scale mechanics – the quasicontinuum method. Journal of the Mechanics and Physics of Solids 47:611–642
129. Tadmor EB, Miller R, Phillips R, Ortiz M (1999) Nanoindentation and incipient plasticity. Journal of Materials Research 14:2233–2250
130. Miller R, Ortiz M, Phillips R, Shenoy V, Tadmor EB (1998) Quasicontinuum models of fracture and plasticity. Engineering Fracture Mechanics 61:427–444
131. Miller R, Tadmor EB, Phillips R, Ortiz M (1998) Quasicontinuum simulation of fracture at the atomic scale. Modelling and Simulation in Materials Science and Engineering 6:607–638
132. Park HS, Karpov EG, Liu WK, Klein PA (2005) The bridging scale for two-dimensional atomistic/continuum coupling. Philosophical Magazine 85:79–113
133. Wagner GJ, Liu WK (2003) Coupling of atomistic and continuum simulations using a bridging scale decomposition. Journal of Computational Physics 190:249–274
134. Qian D, Wagner GJ, Liu WK (2004) A multiscale projection method for the analysis of carbon nanotubes, Computer Methods in Applied Mechanics and Engineering 193:1603–1632
135. Belytschko T, Xiao SP (2003) Coupling methods for continuum model with molecular model. International Journal for Multiscale Computational Engineering 1:115–126

136. Ke CH, Espinosa HD (2005) Numerical analysis of nanotube-based NEMS devices – Part I: Electrostatic charge distribution on multiwalled nanotubes. Journal of Applied Mechanics–Transactions of the ASME 72:721–725
137. Ke CH, Espinosa HD, Pugno N (2005) Numerical analysis of nanotube based NEMS devices – Part II: Role of finite kinematics, stretching and charge concentrations. Journal of Applied Mechanics – Transactions of the ASME 72:726–731
138. Pugno N, Ke CH, Espinosa HD (2005) Analysis of doubly clamped nanotube devices in the finite deformation regime. Journal of Applied Mechanics – Transactions of the ASME 72:445–449
139. Dequesnes M, Tang Z, Aluru NR (2004) Static and dynamic analysis of carbon nanotube-based switches. Journal of Engineering Materials and Technology – Transactions of the ASME 126:230–237
140. Lennard-Jones JE (1930) Perturbation problems in quantum mechanics. Proceeding of the Royal Society of London Series A 129:598–615
141. Girifalco LA, Hodak M, Lee RS (2000) Carbon nanotubes, buckyballs, ropes, and a universal graphitic potential. Physical Review B 62:13104–13110
142. Girifalco LA (1992) Molecular-Properties of C-60 in the Gas and Solid-Phases Journal of Physical Chemistry 96:858–861
143. Hayt WABJ (2001) Engineering Electromagnetics, 6th edn. New York, McGraw-Hill
144. Lou L, Nordlander P, Smalley RE (1995) Fullerene nanotubes in electric-fields. Physical Review B 52:1429–1432
145. Krcmar M, Saslow WM, Zangwill A (2003) Electrostatics of conducting nanocylinders. Journal of Applied Physics 93:3495–3500
146. Rotkin SV, Bulashevich KA, Aluru NR (2002) Atomistic capacitance of a nanotube electromechanical device. International Journal of Nanoscience 1:337–346
147. Bulashevich KA, Rotkin SV (2002) Nanotube devices: A microscopic model. JEPT Letters 75:205–209
148. Keblinski P, Nayak SK, Zapol P, Ajayan PM (2002) Charge distribution and stability of charged carbon nanotubes. Physical Review Letters 89:255503
149. Smythe WR (1956) Charged Right Circular Cylinder. Journal of Applied Physics 27:917–920
150. Yakobson BI, Campbell MP, Brabec CJ, Bernholc J (1997) High strain rate fracture and C-chain unraveling in carbon nanotubes. Computational Materials Science 8:341–348
151. Liu WK, Karpov EG, Park HS (2006) Nano Mechanics and Materials: Theory, Multiscale Methods and Applications. New York, Wiley